buildings

MDPI

Article

Nonlinear Seismic Responses of Near-Fault Building Clusters Caused by the Fault Rupture

Wei Zhong [1,*], Tielin Liu [2], Zhanyuan Zhu [1], Bo Qian [1] and Panli You [1]

[1] School of Civil and Hydraulic Engineering, Xichang University, Xichang 615000, China
[2] School of Civil Engineering, Shenyang Jianzhu University, Shenyang 110168, China
* Correspondence: jonewore@163.com; Tel.: +86-834-2580032

Abstract

An integrated numerical method is proposed for analyzing the nonlinear seismic response of near-fault building clusters, comprising three algorithms: (1) a structural investigated lump algorithm for elastoplastic dynamic response of structure; (2) a connecting investigated lump algorithm for bidirectional wave propagation between the site and elastoplastic building clusters; (3) a geomedia investigated lump algorithm for seismic wave propagation with an improved viscoelastic constitutive model, which allows independent definition of P/S-wave quality factors to characterize geomedia attenuation. Validated for its capability in simulating site-city dynamic interaction problems via a shaking table test, the method is applied to study the seismic response of near-fault building clusters in Xichang City under a hypothetical M_w6.8 earthquake. It is shown that irrespective of whether shallow geological structures are considered, clusters (c2–c4) situated in rupture-forward surface area within ~1.5 km of the fault trace entered the elastoplastic stage, while others (c1, c5) remained elastic. Shallow geological structures may reverse locally hanging-wall/footwall effects of both near-fault structural seismic response and ground motion. A notable seismic-response characteristic of near-fault structures undergoing the elastoplastic stage is that the permanent structural motion displacement (PSMD) at the slab of a specific floor incorporates not only the non-zero permanent ground motion displacement (PGMD) but also the non-zero final structural residual displacement (FSRD) relative to the supporting ground. The developed method could provide support for seismic damage assessment, site selection, and structural optimization design of near-fault building clusters.

Keywords: nonlinear seismic response; near-fault; building cluster; site-city interaction; investigated lump

Check for updates

Academic Editor: Tiago Miguel Ferreira

Received: 20 March 2026
Revised: 24 April 2026
Accepted: 27 April 2026
Published: 29 April 2026

Copyright: © 2026 by the authors. Licensee MDPI, Basel, Switzerland. This article is an open access article distributed under the terms and conditions of the Creative Commons Attribution (CC BY) license.

1. Introduction

In recent decades, numerous densely populated cities worldwide have suffered devastating earthquakes, such as the 1976 Tangshan event [1], 1995 Kobe earthquake [2], 1994 Northridge earthquake [3], and 2023 Türkiye earthquake [4]. Such seismic disasters have induced heavy casualties, substantial economic losses, and extensive structural failure in urban building clusters, further disrupting urban operations and infrastructure. Seismic damage to building groups has become a major trigger of modern urban catastrophic risks. Accordingly, systematic investigation on the seismic performance of urban building clusters is theoretically essential and practically urgent. It helps clarify disaster mechanisms, optimize seismic assessment methods, and support the scientific formulation of urban earthquake prevention, disaster mitigation, and resilience improvement strategies.

Naturally, it is advisable for a reasonable calculation model to account for the actual existence of urban building clusters. Since 1996, many scholars have combined superstructure-building clusters with an underlying geotechnical medium to study site-city interaction (SCI) by using the plane-wave input approach at the bedrock (e.g., refs. [5–18]). From the perspective of structural model selection for urban building groups, existing studies mainly adopt six modeling schemes: (1) low-wave-velocity elastic homogeneous continuous block model [5–11], (2) elastic single-oscillator model [12], (3) equivalent homogeneous elastic continuous cantilever beam model [13], (4) refined elastic finite element model [14], (5) elastic shear/flexural-shear inter-story model [15], and (6) nonlinear shear/flexural-shear inter-story model [16–18]. The first three schemes merely account for the presence of surface buildings, without enabling the calculation of structural internal forces and deformations. The fourth and fifth schemes can obtain elastic structural responses of internal forces and deformation, but cannot reflect building damage and seismic performance. By comparison, the sixth scheme is capable of capturing structural elastoplastic responses and reasonably characterizing seismic damage to buildings. Accordingly, in urban seismic research coupling building clusters and geotechnical media, an inevitable development trend is that structural models evolve from simplified idealized forms to realistic representations, and from linear elastic assumptions to nonlinear deformation descriptions. This scientific research approach, which couples building groups and geotechnical media and adopts plane-wave excitation at the bedrock, may be particularly suitable for far-field (fault distance > 20 km) urban earthquake research.

Actually, a single earthquake's impact zone often could include not only far-field cities but also numerous near-fault (fault distance $\leq$ 20 km) cities. Strong ground motion in near-fault urban areas has distinct features compared to far-field regions, such as the hanging-wall/footwall effect, large-velocity-pulse effect, permanent displacement, and the fault-rupture directivity effect [19–23]. These near-fault ground-motion features, which are mainly driven by fault rupture, may result in more severe earthquake damage to the structures [24–26]. Thus, when studying near-fault urban seismic problems, the fault and its rupture process cannot be overlooked. Specifically, a robust calculation model for analyzing the seismic response of near-fault building clusters should include three essential components: urban building clusters, the earth media, and a seismic source simulating the fault-rupture process. This type of calculation model can also be named the integrated system.

Initially, in the integrated system, the seismic source was treated as a double-couple point source, and the city was simplified to a set of reduced building clusters, which are composed of "low wave-velocity continuous homogeneous blocks" or "single oscillators" [27–29]. Although this single double-couple point source accounts for the actual existence of faults, it cannot simulate the fault-rupture process and is generally suitable for simulating near-fault seismic problems during small earthquakes. In these studies, the researchers investigated SCI considering the earth medium with a flat free surface. The results show that the building cluster's impact on ground motion becomes significant in cities, especially within ~300 m of the cluster. Compared with the scenario without SCI, the structural response amplitude is reduced by roughly 3 times when SCI is considered.

Later, in the integrated system, the seismic source adopted a finite fault model with the fault-rupture process implemented, and the urban building clusters were composed of structure models, simplified as "low wave-velocity continuous homogeneous blocks" [30–32]. Guidotti et al. [30] studied the SCI problem during the 2011 Christchurch earthquake in New Zealand by employing SPEED software. A flat surface was adopted for the free surface of the earth's medium. The results show that seismic waves in cities are significantly affected by building clusters. Buildings do not just play a passive role; they also act as

active sources of numerous closely linked translational and rotational motions. In areas with dense infrastructure, building clusters exert a major influence on the spatial variability of ground motion. Isbiliroglu (2013) and Isbiliroglu et al. (2015) [31,32] investigated the SCI effect during an earthquake by adopting the finite element method. The free surface of the earth's medium was assumed to be a flat surface. The results show that during an earthquake, the SCI effect has a significant impact on the response of building structures. Generally, the SCI effect reduces the structural response; however, in some cases, it may also increase the response. The presence of adjacent buildings can exert a notable influence on the response of individual buildings, especially at high frequencies. In high-density urban areas and regions with distributed soft soil layers, the SCI effect is likely to be highly significant.

From the above research on near-fault urban earthquake problems [27–32], two points are clear: on the one hand, the "buildings" in the urban structure clusters are not real buildings. Obviously, the building group models they used cannot obtain the actual seismic responses of structures (such as structural axial force, shear force, bending moment, and inter-story drift ratio (IDR)). On the other hand, these studies mainly focus on the impact of the existence of urban "building clusters" on ground motion during earthquakes. This is not the seismic response of structure clusters that we focus on in structural engineering.

To obtain the seismic responses of actual structures, in our previous works [33–36], we adopted different structural models and focused on the actual seismic response of near-fault building clusters due to causative fault rupture, achieving some preliminary results. In our integrated system, for individual buildings in the structure clusters, three types of elastic structural models were employed: shear-type multi-story buildings, beam-column frame structures, and flexure-shear high-rise buildings; the constitutive equations for the earth medium included the linear elastic model and the viscoelastic model; the fault rupture process was simulated using a finite-fault kinematic source model. For the viscoelastic model, the generalized Zener body (GZB) relaxation functions for dilatational deformation and shear deformation were used.

However, as seen in the aforementioned studies [33–36], these works only account for the elastic deformation of building structure clusters, while omitting the elastoplastic deformation that is inherently associated with the development of earthquake damage in real urban structures. In other words, the used building cluster models fail to capture the nonlinear behavior of structures subsequent to elastic deformation, and further cannot illustrate the failure process or seismic damage characteristics of near-fault urban structure clusters during an earthquake.

Collectively, existing studies, including our previous work, have laid an important foundation for the seismic response analysis of near-fault building clusters, yet still suffer from critical limitations. Although remarkable progress has been made by scholars worldwide in near-fault ground motion effects on building structures (e.g., refs. [37–41]), linear and nonlinear soil-structure interaction (SSI) (e.g., refs. [42–44]), linear and nonlinear structure-soil-structure interaction (SSSI) (e.g., refs. [45–48]), SCI (e.g., refs. [49,50]), and urban seismic resilience (e.g., refs. [18,51]), most computational models either adopt direct ground motion input at structural supports (e.g., refs. [37–41,48]), or apply plane-wave input at bedrock (e.g., refs. [42–47,49,50]), or consider a single structure (e.g., refs. [42–44]), or still employ elastic structural assumptions (e.g., refs. [42,45,46]). Few studies have fully integrated fault rupture process, viscoelastic wave propagation, SCI, and structural elastoplasticity into a unified nonlinear analysis framework. In particular, such integrated studies remain extremely scarce for near-fault mountainous cities with complex shallow geological conditions. Therefore, this paper presents an exploratory study, hoping to provide use-

ful insights and methodological references for the nonlinear seismic response analysis of near-fault building clusters.

The purpose of this paper is to develop a new integrated simulation method for the nonlinear seismic response of near-fault elastoplastic building clusters in mountainous cities, which accounts for the fault-rupture process. Furthermore, the developed method is applied to study the seismic response of Xichang City during an M_w6.8 hypothetical earthquake. First, in Section 2.1, based on the idea and concept of the investigated lump [34,52], a structural investigated-lump algorithm capable of analyzing the elastoplastic dynamic response of building structures is proposed. In contrast to previous studies [33–36] that employed elastic structural models, this paper adopts an elastoplastic structural model to account for structural nonlinearity. Second, in Section 2.2 and Appendix A, a geomedia investigation of a lump algorithm is developed for simulating viscoelastic wave propagation using the *P*-wave and *S*-wave GZB relaxation functions, which allows independent definition of *P*-wave and *S*-wave quality factors. The parameters of this type of viscoelastic constitutive equation can be directly obtained from the quality factors of *P*-waves and *S*-waves. This differs from our previous studies [34,35], where the viscoelastic constitutive equations adopt the dilatational-deformation and shear-deformation GZB relaxation functions. The parameters can only be indirectly obtained from the quality factors of *P*-waves and *S*-waves. Meanwhile, a connecting investigated-lump algorithm is developed for bidirectional wave propagation between the site and elastoplastic structures. The structural investigated lump algorithm, the geomedia investigated lump algorithm, and the connecting investigated lump algorithm constitute the integrated method developed in this study, which achieves the fault rupture propagation, SCI, and structural nonlinearity. Then, in Section 3, a numerical verification example is provided, and its results are compared with experimental data to validate the effectiveness and correctness of the developed method in solving site-city dynamic interaction problems. Finally, in Section 4, the developed integrated numerical method is applied to simulate the nonlinear seismic responses of near-fault building clusters at different mountainous locations in Xichang City during an M_w6.8 hypothetical earthquake in the Anninghe Fault Zone. The influences of shallow geological structures on the seismic response of near-fault building clusters and on near-fault ground motion, along with the influence of structural nonlinearity on the seismic response of these clusters, are studied in this work.

2. Numerical Method

Figure 1 shows the investigated lumps and their construction process in the integrated system for obtaining nonlinear earthquake responses of near-fault building clusters. The integrated system is composed of building clusters with elastoplastic deformation capacity, a viscoelastic earth medium, and a causative fault, as shown in Figure 1a. Taking the frame structure shown in Figure 1b as an example, the construction process of the three types of investigated lumps is illustrated. They are respectively the structural investigated lump (Figure 1c), the connecting investigated lump (Figure 1d), and the geomedia investigated lump (Figure 1d). For more details of the construction process, please also refer to our previous works [34,35]. The algorithm implementation of the structural and connecting investigated lumps will be described in Sections 2.1 and 2.2. As for the case of the geomedia investigated lump, please see the literature [34].

To understand the dynamic governing equations of the investigated lumps in the following Section 2.1 easily, the main symbols need to be explained in advance. The symbol l (e.g., the number ① shown in Figure 1b) denotes the number of the lth inter-story segment with the upper endpoint, f_{l+1}, and the lower endpoint, f_l, $l = 1, \ldots, L$, where L is the total number of building stories. Among these endpoints f_1 through f_{l+1}, point f_1 represents

the position of the ground surface at soil-structure connection, and the investigated lump at the point f_1 is also termed the connecting investigated lump f_1; point f_{l+1} denotes the position of the $(l+1)$th-floor slab point ($l < L$) or the roof slab point ($l = L$) in the structure; the investigated lump at point f_{l+1} is also referred to as the structural investigated lump f_{l+1}. h_l is the lth-floor height.

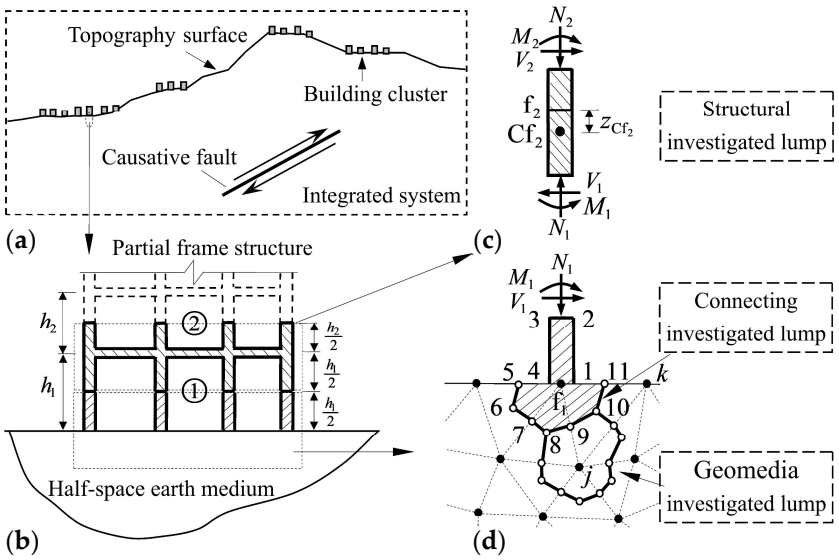


Figure 1. Investigated lumps in the integrated system for simulating nonlinear seismic responses of near-fault building clusters induced by the causative fault rupture. (**a**) The integrated system including building clusters with elastoplastic deformation capacity, viscoelastic earth medium with topography surface, and causative fault. (**b**) A typical frame structure in the building clusters. (**c**) A typical structural investigated lump. (**d**) A typical connecting investigated lump and a typical geomedia investigated lump.

2.1. Algorithm Implementation of Nonlinear Dynamic Response for Structure

Considering a typical structural investigated lump f_{l+1} (e.g., the structurally investigated lump f_2 shown in Figure 1c), according to its force analysis (referring to Figure 1c), and using the mass damping coefficient β_1 for Rayleigh damping, the dynamic equilibrium equations at the centroid Cf_{l+1} of the investigated lump f_{l+1} are obtained as follows

$$m_{f_{l+1}}\ddot{u}_{Cf_{l+1}} = V_{l+1} - V_l - \beta_1 m_{f_{l+1}}\dot{u}_{f_{l+1}} \tag{1}$$

$$m_{f_{l+1}}\ddot{w}_{Cf_{l+1}} = (N_l - N_{l+1}) - m_{f_{l+1}}g - \beta_1 m_{f_{l+1}}\dot{w}_{f_{l+1}} \tag{2}$$

$$\begin{aligned} J_{Cf_{l+1}}\ddot{\theta}_{Cf_{l+1}} &= (M_{l+1} - M_l) + V_{l+1}\left(\frac{h_{l+1}}{2} + z_{Cf_{l+1}}\right) + V_l\left(\frac{h_l}{2} - z_{f_{l+1}}\right) \\ &+ N_{l+1}\left(\frac{u_{f_{l+2}} - u_{f_{l+1}}}{2} + z_{f_{l+1}}\frac{u_{f_{l+1}} - u_{f_l}}{h_l}\right) \\ &+ N_l\left(\frac{u_{f_{l+1}} - u_{f_l}}{2} - z_{Cf_{l+1}}\frac{u_{f_{l+1}} - u_{f_l}}{h_l}\right) - \beta_1 J_{Cf_{l+1}}\dot{\theta}_{Cf_{l+1}} \end{aligned} \tag{3}$$

where it should be pointed out that $V_{L+1} = 0$, $N_{L+1} = 0$ and $M_{L+1} = 0$. The $m_{f_{l+1}}$ and $J_{Cf_{l+1}}$ are respectively the mass of the structurally investigated lump f_{l+1} and its moment of inertia through its centroid Cf_{l+1} around the y-axis. The mass damping coefficient β_1 for Rayleigh damping, it can be determined by using $\beta_1 = 2\omega_1\omega_2(\zeta_1\omega_2 - \zeta_2\omega_1)/(\omega_2^2 - \omega_1^2)$, ω_1 and ω_2 are respectively the first- and second-order circular natural frequencies for the structure, ζ_1 and ζ_2 the first and second modal damping ratios for the structure are often set as $\zeta_1 = \zeta_2 = 0.05$ [53,54].

The "one dot" and "two dots" above the displacements $u_{\mathrm{Cf}_{l+1}}$, $w_{\mathrm{Cf}_{l+1}}$ and $\theta_{\mathrm{Cf}_{l+1}}$ represent respectively the first-order and second-order derivative with respect to time for the corresponding displacements, i.e., the velocity and acceleration. $z_{\mathrm{Cf}_{l+1}}$ is the eccentricity of $(l+1)$th-floor slab surface point f_{l+1} of the structural investigated lump f_{l+1} relative to its centroid Cf_{l+1}. g is the gravity acceleration. To calculate the $\ddot{u}_{\mathrm{Cf}_{l+1}}$, $\ddot{w}_{\mathrm{Cf}_{l+1}}$ and $\ddot{\theta}_{\mathrm{Cf}_{l+1}}$, the mid-section interior forces V_l (V_{l+1}), N_l (N_{l+1}) and M_l (M_{l+1}) for the lth ($(l+1)$th) inter-story segment need to be determined. Actually, the calculation formulae of V_{l+1}, N_{l+1} and M_{l+1} are similar to those of V_l, N_l and M_l. So, only the calculation formulae of V_l, N_l and M_l are given in this study.

For the calculation formula of the V_l, a bilinear hysteretic kinematic hardening model will be used to approximately characterize the nonlinear relationship between mid-section shear force V_l and shear-displacement Δu_l for the lth inter-story segment. Figure 2 shows this model for the lth inter-story segment. The Δu_l^e represents the inter-story shear-displacement corresponding to the elastic limit and $\Delta u_l^e = h_l/550$ for R/C frame structure according to the current China Code for Seismic Design of Buildings (GB 50011-2010) [54].

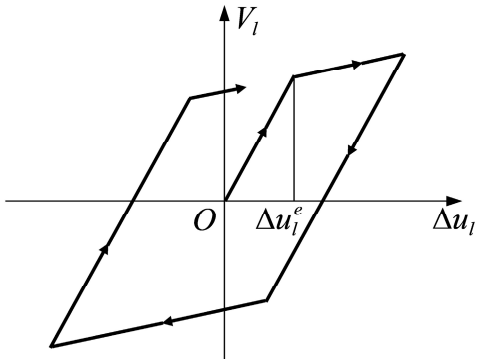


Figure 2. The bilinear hysteretic kinematic hardening model of mid-section shear force V_l and shear-displacement Δu_l for the lth inter-story segment. The Δu_l^e denotes the inter-story shear-displacement corresponding to structural elastic limit.

After considering the influence of axial force N_l on the V_l and using stiffness damping coefficient β_2 for Rayleigh damping as well as employing the incremental theory, the formulas of shear force V_l^t at time t is obtained as follows

$$V_l^t = V_l^{t-\Delta t} + K_{1l}^t\left(\Delta u_l^t - \Delta u_l^{t-\Delta t}\right) - \frac{N_l^t}{2}\left(\theta_{\mathrm{f}_l}^t + \theta_{\mathrm{f}_{l+1}}^t\right) + \frac{N_l^{t-\Delta t}}{2}\left(\theta_{\mathrm{f}_l}^{t-\Delta t} + \theta_{\mathrm{f}_{l+1}}^{t-\Delta t}\right)$$
$$+\beta_2 K_{1l}^t\left(\Delta \dot{u}_l^t - \Delta \dot{u}_l^{t-\Delta t}\right) - \beta_2\frac{N_l^t}{2}\left(\dot{\theta}_{\mathrm{f}_l}^t + \dot{\theta}_{\mathrm{f}_{l+1}}^t\right) + \beta_2\frac{N_l^{t-\Delta t}}{2}\left(\dot{\theta}_{\mathrm{f}_l}^{t-\Delta t} + \dot{\theta}_{\mathrm{f}_{l+1}}^{t-\Delta t}\right) \quad (4)$$

where the Δt is time step and the inter-story shear-displacement Δu_l is expressed as $\Delta u_l = \left(u_{\mathrm{f}_{l+1}} - u_{\mathrm{f}_l}\right) - 0.5\left(\theta_{\mathrm{f}_{l+1}} + \theta_{\mathrm{f}_l}\right)h_l$. K_{l1}^t is the lateral displacement stiffness of the lth story at time t, $K_{l1}^t = K_{le}^t = 12(EI)_l/\left[(1+2\alpha_l)h_l^3\right] - 6N_l^t/(5h_l)$ (elastic stage) and $K_{l1}^t = K_{lp}^t = \eta K_{le}^t$ (hardening stage), η is plastic stiffness coefficient, typically in the range of 1/20–1/10 [55–57]. The α_l is coefficient of shear deformation for the lth inter-story segment and $\alpha_l = 6(EI)_l/\left[h_l^2(GA_s)_l\right]$. The stiffness damping coefficient β_2 for Rayleigh damping can be calculated by using $\beta_2 = 2(\zeta_2\omega_2 - \zeta_1\omega_1)/\left(\omega_2^2 - \omega_1^2\right)$ [53].

As for the calculation formulas of the N_l and M_l, considering structural linear elastic deformation, we can obtain them as follows

$$N_l = \frac{(EA)_l}{h_l}(w_{\mathrm{f}_l} - w_{\mathrm{f}_{l+1}}) + N_{gl} + \beta_2\frac{(EA)_l}{h_l}\left(\dot{w}_{\mathrm{f}_l} - \dot{w}_{\mathrm{f}_{l+1}}\right) \quad (5)$$

$$M_l = \frac{(EI)_l}{h_l}(\theta_{\mathrm{f}_{l+1}} - \theta_{\mathrm{f}_l}) + \beta_2 \frac{(EI)_l}{h_l}(\dot{\theta}_{\mathrm{f}_{l+1}} - \dot{\theta}_{\mathrm{f}_l}) \tag{6}$$

where N_{gl} is the mid-section axial force of the lth inter-story segment due to its dead-weight.

From Equations (4)–(6), the mid-section interior forces of the lth inter-story segment can be calculated from the displacements and velocities at the points f_l and f_{l+1}. Clearly, these displacements and velocities can be obtained from accelerations at the points f_l and f_{l+1} by doing time integration. The accelerations used here at all points f_1-f_{L+1} originate from different investigated lumps. The acceleration at the point f_1 comes from connecting investigated lump f_1 as will be illustrated in Section 2.2; the accelerations at the point f_{l+1} structural investigated lump f_{l+1}. But the accelerations obtained from Equations (1)–(3) are ones at the centroid point Cf_{l+1} of each structural investigated lump. Therefore, it needs to establish the relationship between accelerations at the point f_{l+1} and ones at the centroid point Cf_{l+1}. According the kinematical theory, we can obtain the accelerations at the point f_{l+1} as follows

$$\ddot{u}_{\mathrm{f}_{l+1}} = \ddot{u}_{\mathrm{Cf}_{l+1}} + z_{\mathrm{Cf}_{l+1}}\ddot{\theta}_{\mathrm{Cf}_{l+1}} \tag{7}$$

$$\ddot{w}_{\mathrm{f}_{l+1}} = \ddot{w}_{\mathrm{Cf}_{l+1}} - z_{\mathrm{Cf}_{l+1}}\dot{\theta}^2_{\mathrm{Cf}_{l+1}} \tag{8}$$

$$\ddot{\theta}_{\mathrm{f}_{l+1}} = \ddot{\theta}_{\mathrm{Cf}_{l+1}} \tag{9}$$

The aforementioned Equations (1)–(9) constitute the governing equations of the nonlinear dynamic response of the structure. Its algorithm is implemented in a time-domain recursive way as follows:

Step (1) Calculate $\ddot{u}_{\mathrm{Cf}_{l+1}}$, $\ddot{w}_{\mathrm{Cf}_{l+1}}$ and $\ddot{\theta}_{\mathrm{Cf}_{l+1}}$ of structural investigated lump f_{l+1} at time t by using Equations (1)–(3).

Step (2) Calculate $\dot{u}_{\mathrm{Cf}_{l+1}}$, $\dot{w}_{\mathrm{Cf}_{l+1}}$ and $\dot{\theta}_{\mathrm{Cf}_{l+1}}$ of structural investigated lump f_{l+1} at time $t + \Delta t/2$ for damping forces in Equations (1)–(3) by doing once time integration.

Step (3) Calculate $\ddot{u}_{\mathrm{f}_{l+1}}$, $\ddot{w}_{\mathrm{f}_{l+1}}$ and $\ddot{\theta}_{\mathrm{f}_{l+1}}$ of structural investigated lump f_{l+1} at time t by using Equations (7)–(9).

Step (4) Calculate $\dot{u}_{\mathrm{f}_{l+1}}$, $\dot{w}_{\mathrm{f}_{l+1}}$ and $\dot{\theta}_{\mathrm{f}_{l+1}}$ of structural investigated lump f_{l+1} at time $t + \Delta t/2$ by doing one-time integration and $u_{\mathrm{f}_{l+1}}$, $w_{\mathrm{f}_{l+1}}$ and $\theta_{\mathrm{f}_{l+1}}$ at time $t + \Delta t$ by doing twice the time integration.

Step (5) Calculate the middle cross-section interior forces V_l, N_l and M_l of the lth inter-story segment at time $t + \Delta t$ in the structure by using Equations (4)–(6).

Step (6) Return to step (1) to update the $\ddot{u}_{\mathrm{Cf}_{l+1}}$, $\ddot{w}_{\mathrm{Cf}_{l+1}}$ and $\ddot{\theta}_{\mathrm{Cf}_{l+1}}$ of structural investigated lump f_{l+1} at time $t + \Delta t$.

Through the above time-domain recursive calculating process, the algorithm for the nonlinear response of the structure will be implemented.

It should be pointed out that the P-Δ effects (geometric nonlinearity) have been incorporated to account for second-order effects under deformations, while the stiffness degradation, strength deterioration, and cumulative damage effects associated with repeated cyclic loading are not incorporated in the current constitutive model. This is because the main focus of this study is to establish an integrated numerical framework for coupled wave propagation, soil-structure interaction, and structural elastoplastic response, and a bilinear hysteretic model without degradation is sufficiently accurate for characterizing the main nonlinear behavior of structures. Cumulative damage is subsequently evaluated using IDR-based damage indices.

2.2. Algorithm Implementation for Wave Bidirectional Propagation at the Soil-Structure Connection

As is depicted in Figure 1d, the shaded part enclosed by 1→2→3→4→5→6→7→8→9→10→11→1 is the connecting investigated lump f_1, which is composed of the corresponding investigated lump at the surface of the earth media and the half-length of the 1st inter-story segment in the structure. According to its force analysis, the dynamic equilibrium equations of the connecting investigated lump f_1 with mass m_{f_1} and moment of inertia J_{f_1} are given as follows

$$m_{f_1}\ddot{u}_{f_1} = \sum_{n=1}^{n_{f1}}(\sigma_{xx})_n(a'_{f_1})_n - \sum_{n=1}^{n_{f1}}(\sigma_{xz})_n t(b'_{f_1})_n + V_1 \tag{10}$$

$$m_{f_1}\ddot{w}_{f_1} = \sum_{n=1}^{n_{f1}}(\sigma_{xz})_n(a'_{f_1})_n - \sum_{n=1}^{n_{f1}}(\sigma_{zz})_n(b'_{f_1})_n - N_1 \tag{11}$$

$$J_{f_1}\ddot{\theta}_{f_1} = M_1 + \frac{1}{2}V_1 h_1 \tag{12}$$

where n_{f_1} is the number of triangular grids around the surface node f_1 of earth media. For a typical triangle $f_1 - j - k$, $a'_{f_1} = (z_k - z_j)/2$, $a'_j = (z_{f_1} - z_k)$, $a'_k = (z_j - z_{f_1})/2$, $b'_{f_1} = (x_k - x_j)/2$, $b'_j = (x_{f_1} - x_k)/2$, $b'_k = (x_j - x_{f_1})/2$, $(x_i,\ z_i)$ $(i = f_1,\ j,\ k)$ is the coordinate of the triangular three nodes. To calculate $\ddot{u}_{f_1}$, $\ddot{w}_{f_1}$ and $\ddot{\theta}_{f_1}$, stress components σ_{xx}, σ_{zz} and σ_{xz} need to be determined.

The stress components σ_{xx}, σ_{zz} and σ_{xz} in Equations (10)–(12) can be evaluated by using Equations (A19)–(A24) in Appendix A.

The Equations (10)–(15), (A19)–(A24) and (4)–(6) constitute the governing equations of wave bidirectional propagation at the soil-structure connection. Its algorithm is implemented in a time-domain recursive way as follows:

Step (1) Calculate $\ddot{u}_{f_1}$, $\ddot{w}_{f_1}$ and $\ddot{\theta}_{f_1}$ of connecting the investigated lump f_1 at time t by using Equations (10)–(12).

Step (2) Calculate u_{f_1}, w_{f_1} and θ_{f_1} at time $t + \Delta t$ by doing twice the time integration.

Step (3) Calculate σ_{xx}, σ_{zz} and σ_{xz} at time $t + \Delta t$ by using Equations (A19)–(A24).

Step (4) Calculate the middle cross-section interior forces V_1, N_1 and M_1 of the first inter-story segment at the time $t + \Delta t$ in the structure by using Equations (4)–(6).

Step (5) Return to Step (1) to update the $\ddot{u}_{f_1}$, $\ddot{w}_{f_1}$ and $\ddot{\theta}_{f_1}$ of connecting the investigated lump f_1 at time $t + \Delta t$.

Through the above time-domain recursive calculation process, the algorithm for wave bidirectional propagation between soil and each structure in building clusters will be implemented.

As for the algorithm for viscoelastic wave propagation in the Earth's medium, it has been introduced in our previous work [34]. But it should be pointed out that the viscoelastic constitutive equations used herein are different from those used in our previous work [34]. The relaxation function used by the former accounts for the GZB's *P*-wave tension-compression and *S*-wave shear viscoelastic behavior, while the relaxation function adopted by the latter considers the GZB's dilatational and shear viscoelastic behavior. Compared with the case of the latter, the former can independently define the *P*-wave and *S*-wave quality factors, and the viscoelastic parameters can be directly obtained from the constant *P*-wave and *S*-wave quality factors.

The aforementioned algorithms based on the investigated lump concept have the following advantages:

(1) The structurally investigated lump algorithm features a clear physical meaning and straightforward implementation. It is formulated based on the dynamic equilibrium of structurally investigated lumps. The dynamic response analysis of the structure can

be realized simply by performing a force analysis and establishing the corresponding governing dynamic equations.

(2) The connecting investigated lump algorithm naturally incorporates SSI, SSSI, SCI, and other phenomena. This approach realizes the wave-based soil-structure connection by enforcing dynamic equilibrium at every time instant for each soil-structure connecting investigated lump.

(3) The geomedia investigated the lump algorithm, which exhibits high computational efficiency, naturally satisfies free boundary conditions, and can flexibly handle irregular topography and irregular internal interfaces. It combines the advantages of the finite difference method (high computational efficiency), the finite element method (natural satisfaction of free-boundary conditions), and an unstructured triangular auxiliary grid (flexibility in dealing with irregular topography and interfaces) [52].

In summary, the above three algorithms, including the elastoplastic structural investigated lump algorithm, the connecting investigated lump algorithm for wave bidirectional propagation, and the viscoelastic geomedia investigated lump algorithm, form a complete integrated simulation method in this study by introducing the finite-fault seismic source. The main feature is that it combines elastoplastic structural dynamics, viscoelastic wave propagation, fault-rupture processes, and site-city dynamic interaction into a unified nonlinear framework, which is beneficial for the nonlinear seismic response analysis of near-fault building clusters in mountainous cities.

3. Verification of the Developed Numerical Method

To validate the effectiveness of the presented numerical method in handling site-city dynamic interaction, a shaking table test [58] is selected for comparative verification. Figure 3 shows the calculation model of the shaking table test. There is an idealized small-scale city constituting 37 identical resonating structures, distributed equally, with a center-to-center spacing of 50 mm at the flat surface of the underlying soil. Each structure is simulated by using an aluminum sheet with a height of 184 mm and a thickness of 0.5 mm. The aluminum sheet is characterized by mass density $\rho_{\mathrm{Al}} = 2700\ \mathrm{kg/m^3}$, Young modulus $E_{\mathrm{Al}} = 69 \times 10^9$ Pa and Poisson ratio $v_{\mathrm{Al}} \approx 0.3$. The fundamental frequency and damping ratio of each aluminum sheet respectively are approximately 8.45 Hz and 4%, according to the experimental results. The mass damping coefficient β_1 is 3.66 1/s and the stiffness damping coefficient β_2 is 2.08×10^{-4} s based on the first and second modal damping ratios $\xi_1 = 4\%$ and $\xi_2 = 4\%$ as well as the first and second modal natural angular frequencies $\omega_1 = 53.09$ rad/s and $\omega_2 = 331.83$ rad/s [53,58]. Each aluminum sheet is divided into 10 segments, which construct 11 structurally investigated lumps.

The underlying soil is simulated by using a polyurethane foam block with dimensions of 2.13 m × 0.76 m in xoz plane. The foam's material properties are mass density ρ of 49 kg/m^3, P-wave velocity V_p of 48.98 m/s, S-wave velocity V_s of 33.5 m/s, and shear-deformation damping ratio ξ_s of 4.9%. According to the literature [59,60], the viscoelastic constitutive relationship can be used to characterize the hysteretic damping property of the foam. To be specific, the foam's volumetric deformation follows an elastic relationship (i.e., volumetric-deformation quality factor $Q_k = \infty$, giving $\chi_{pn} = \left(4V_s^2/3V_p^2\right)\chi_{sn}$ [34]), while its shear deformation complies with the GZB viscoelastic relationship. The quality factor Q_s is about 10.2 for S-wave according to $Q_s = 1/(2\xi_s)$ [60], and then the parameters χ_{sn} for S-wave can be obtained from Q_s by the least squares technique [61]. In this study, 1420 triangular auxiliary grids with a spatial step size of 0.05 m are used for constructing 768 geomedia-investigated lumps. The time step is set to 3.0×10^{-6} s and 1,000,000 steps are conducted in total. The computational time is approximately 15 min on a single 2.5 GHz CPU computer.

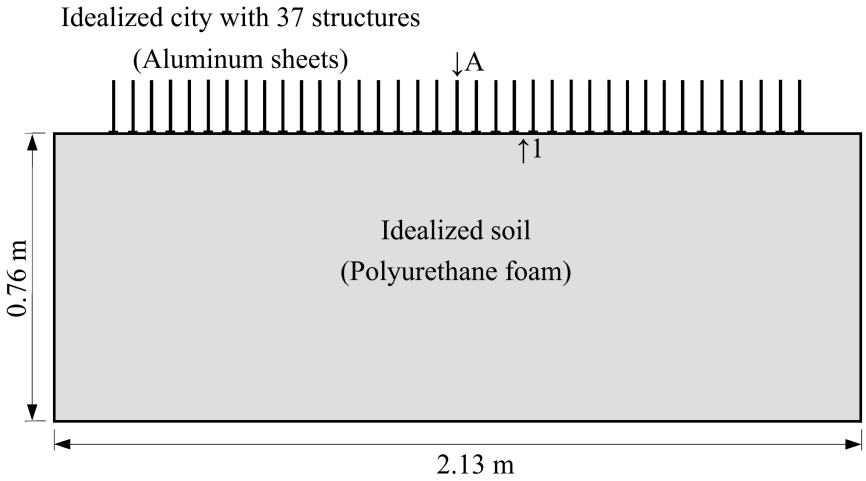


Figure 3. Computational model of the table shaking test. The upward arrow (symbol 1) denotes the receiver located at the midpoint of the ground between the 22nd and 23rd structures. The downward arrow (symbol A) indicates the receiver located at the top of the 19th structure.

To match the boundary conditions similar to the table shaking test, a Ricker acceleration time history with an acceleration peak of 2.55 m/s^2 and a dominant frequency of around 8 Hz is inputted along the x direction on the bottom boundary, while the bottom boundary along the z direction is fixed; the lateral boundaries are free surfaces.

Figure 4 illustrates the response comparison between numerical simulation and shaking table test results for the idealized city (comprising 37 structures), including (a) x-direction acceleration at ground receiver 1 and (b) x-direction acceleration at receiver A on the 19th structure's top. To quantitatively evaluate the consistency between numerical and experimental results, we shall introduce three error indices: the correlation coefficient, root-mean-square error (RMSE), and peak error percentage [62,63]. Among them, the correlation coefficient and RMSE respectively reflect the trend-and-phase consistency and overall deviation between numerical and experimental time histories; the peak error percentage reflects the prediction accuracy of the maximum response amplitude.

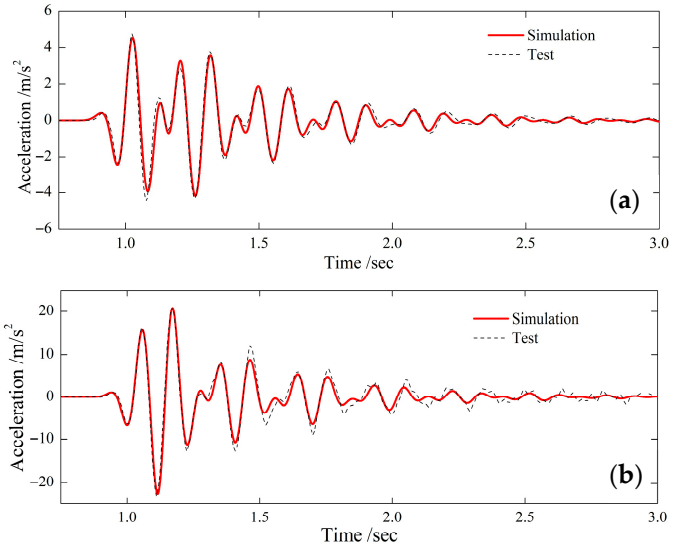


Figure 4. Comparison of responses of idealized city model with 37 structures between the results of numerical simulation and those of shaking table test: (**a**) x-direction acceleration at receiver 1 at the surface of underlying soil; (**b**) x-direction acceleration at receiver A on the top of the 19th structure.

From Figure 4a, the numerical result at the ground receiver 1 is in good agreement with the experimental data. The correlation coefficient reaches 0.976, indicating high consistency in the temporal trend and phase of the acceleration response. The RMSE is 0.233 m/s^2, corresponding to a small overall deviation. The peak acceleration from the simulation is 4.527 m/s^2, with a peak error percentage of only 4.56% with respect to the experimental peak acceleration of 4.743 m/s^2, both well within acceptable ranges for ground motion validation.

From Figure 4b, the numerical result at receiver A on the 19th structure's top generally captures the key features of the experimental response. A correlation coefficient of 0.973 indicates good overall consistency in trend and phase. The simulated peak acceleration is 20.804 m/s^2, with a peak error percentage of only 0.88% relative to the experimental peak acceleration of 20.990 m/s^2, showing excellent peak prediction accuracy. However, an RMSE of 1.045 reveals noticeable discrepancies in the late time history (after approximately 1.25 s), which may arise from the dynamic interaction between the actual three-dimensional soil specimen's front and rear free surfaces and the building cluster, but this type of dynamic interaction is not fully captured in the simulation for the plane strain problem. Overall, the simulation achieves acceptable accuracy for seismic response analysis of building clusters.

These indices collectively confirm that the numerical method accurately captures both the global response evolution and peak amplitude characteristics, demonstrating sufficient reliability for further analysis. It is concluded that the proposed numerical method can efficiently deal with the site-city dynamic interaction problem, which actually includes reliable simulations of seismic wave propagation in a structure cluster and the earth medium as well as bidirectional wave propagation between them.

4. Numerical Simulation

Xichang City is located in the southwestern part of Sichuan Province, China, and is a typical mountainous city near faults. As shown in Figure 5, there are mainly two large fault zones (red thick solid line) through Xichang City: The Anninghe Fault Zone and the Zemuhe Fault Zone [64]. One of the two fault zones, the Anninghe Fault Zone, with a strike of ~0° and a dip angle of ~76°, runs beneath Xichang City [65]. The red thick dashed line represents our selected computational plane, which is perpendicular to the Aninghe Fault trace. Detailed interpretation of fault geomorphic aerial photographs and field surveys indicates that, in addition to the dominant left-lateral strike-slip fault activity, the Anninghe Fault Zone also exhibits a significant reverse-thrust movement component [65–67]. In this study, a hypothetical M_w6.8 earthquake due to rupture of a reverse causative fault in the Anninghe Fault Zone is considered to obtain the nonlinear seismic response of near-fault building clusters in the Xichang Area. Three effects are examined in this research: the influence of shallow geological structures on both the seismic response of near-fault building clusters and near-fault ground motion, as well as the influence of structural nonlinearity on the seismic response of such clusters.

4.1. Computational Model

Figure 6 shows the computational model for the nonlinear seismic response analysis of near-fault building clusters in the Xichang Area during a hypothetical M_w6.8 earthquake in the Anninghe Fault Zone. The computational model includes building clusters, earth media, and causative faults.

As shown in Figure 6, five near-fault building clusters are considered on the Earth's media surface from west to east, namely: c1, c2, c3, c4, and c5. Their center distances to the fault trace are, respectively, as follows: 3.3 km, 1.0 km, 0.0 km, 1.0 km, and 3.3 km. To facilitate analysis, each building cluster comprises 10 identical 3-bay 5-story RC frame

buildings, which are evenly distributed with a center-to-center spacing of 50 m. Each building's planar dimensions are 54 m × 17.7 m. A planar frame structure is considered along the short-axis direction. The planar frame has two external spans of equal length and one inner span. The external span and the internal span are, respectively, 7.5 m and 2.7 m. The floor height per story is 3.6 m, and the building height is 18.0 m. The column and beam cross-sectional dimensions are, respectively, 400 mm × 500 mm and 250 mm × 700 mm. Slab thickness is 120 mm. The concrete grade is C30 with a density of 2500 kg/m^3; the reinforcing steel is grade HRB400 with a density of 7850 kg/m^3. The computational parameters of structural equivalent stiffnesses and structural investigated lumps are listed in Tables 1 and 2, respectively. The first-order natural frequency and second-order natural frequency of the structure are 3.8 Hz and 11.0 Hz, respectively, with a structural damping ratio of 0.05 [54]. Thus, the mass-damping coefficient β_1 and stiff-damping coefficient β_2 for each building are respectively calculated as 1.77 1/s and 1.08 × 10^{-3} s. The inter-story drift limit Δu_l^e at yielding is $h_l/550$ in accordance with GB 50011-2010 [54]. The plastic stiffness coefficient η is set to be 1/10.

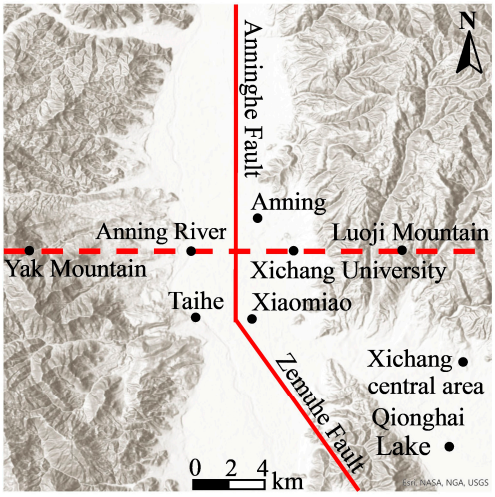


Figure 5. The selected computational plane (red thick dashed line) of Xichang City in this study. It is perpendicular to the strike direction (0°) of the Anninghe Fault, passing through Yak Mountain, Anning River, Xichang University, and Luoji Mountain.

Table 1. The computational parameters of structural equivalent stiffnesses.

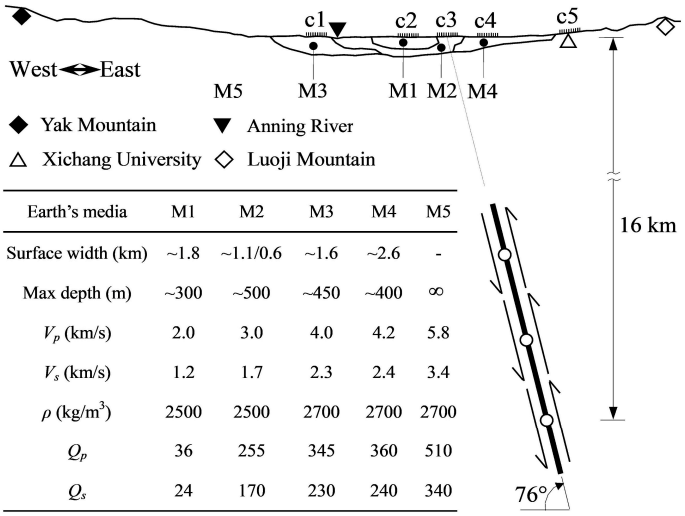
Story No.	Bending Stiffness/×10^9 kN·m^2	Axial Stiffness/×10^7 kN	Shear Stiffness/×10^6 kN
1–5	2.74	6.83	1.58

Table 2. The computational parameters of structural investigated lumps.

Investigated Lump No.	Mass/×10^3 kg	Rotary Inertia/×10^6 kg·m^2
1	9.14	0.38
2–5	68.19	1.68
6	59.06	1.31

A typical feature of the shallow subsurface velocity structures along the Anninghe Fault is the presence of distinct low-velocity zones (LVZs, $V_p \leq 3.5$ km/s), which are mainly formed from a combined result of fault damage zones produced by historical earthquakes and sediments controlled by the Anninghe Fault's tectonic activity [67]. These distinct LVZs generally exhibit a width of approximately 1000–1500 m and a depth of around 300–400 m,

with a *P*-wave velocity ranging from 1.6 to 2.4 km/s, and at least a 31% reduction compared to the surrounding rock high-velocity zones (HVZs, V_p > 3.5 km/s).



Earth's media	M1	M2	M3	M4	M5
Surface width (km)	~1.8	~1.1/0.6	~1.6	~2.6	-
Max depth (m)	~300	~500	~450	~400	∞
V_p (km/s)	2.0	3.0	4.0	4.2	5.8
V_s (km/s)	1.2	1.7	2.3	2.4	3.4
ρ (kg/m^3)	2500	2500	2700	2700	2700
Q_p	36	255	345	360	510
Q_s	24	170	230	240	340

Figure 6. Computational model consisting of building clusters, earth media, and fault for nonlinear seismic response analysis of near-fault building clusters in Xichang Area during a hypothetical M_w6.8 earthquake in Anninghe Fault Zone. The fault trace is situated on the ground of the center of building cluster c3.

In this study, referring to the shallow geological structures beneath the southern array MX3 mentioned in the literature [67], as shown in Figure 6, we consider a simplified shallow geological geometry and velocity structure including a distinct LVZ (M1), an LVZ (M2), and two surrounding HVZs (M3 and M4) into the computational model. The M1 has a surface width of ~1.8 km and a max depth of ~300 m. The M2 has a surface width of ~1.1/0.6 km on the west/east of M1 and a max depth of ~500 m. The M3 is ~1.6 km wide with a max depth of ~450 m, and the M4 is ~2.6 km wide with a max depth of ~400 m. As for the deep geological structure, only a half-space bedrock zone (M5) is considered. The properties of Earth's media are derived from the literature [34,67,68] and listed in the table at the lower left corner of Figure 6.

According to the literature [69], for an M_w6.8 earthquake, the fault strike length and dip width are respectively 33.4 km and 14.0 km, with an optimal subfault size of 5.0 km and three subfaults arranged along the dip direction. The average fault slip and rise time are respectively 0.88 m and 5.07 s. To reflect the inhomogeneous fault distribution, the slip of each subfault is randomly assigned within 0.44–1.32 m and the rise time within 3.04–7.10 s [33,70]. Referring to Song et al. [65], the focal depth is 16 km, and the dip angle is 76°.

In this study, the computational dimension is 50 km × 25 km. A total of 7,458,875 triangular auxiliary grids with a spacing of 10–20 m is employed to construct 3,733,742 geomedia-investigated lumps. The time step is 1.0×10^{-3} s, with 20,000 calculation steps. The simulation lasts about 8.5 h on a single 2.5 GHz CPU computer.

4.2. Numerical Results

4.2.1. The Influence of the Shallow Geological Structure on Seismic Responses of Near-Fault Building Clusters

To explore how shallow geological features affect the seismic responses of near-fault building clusters, two computational models, one with and one without shallow geological structures are established. Figure 7 shows the comparison of peak IDRs of each

structure in five building clusters (c1–c5) for the two cases, with and without the shallow geological structures.

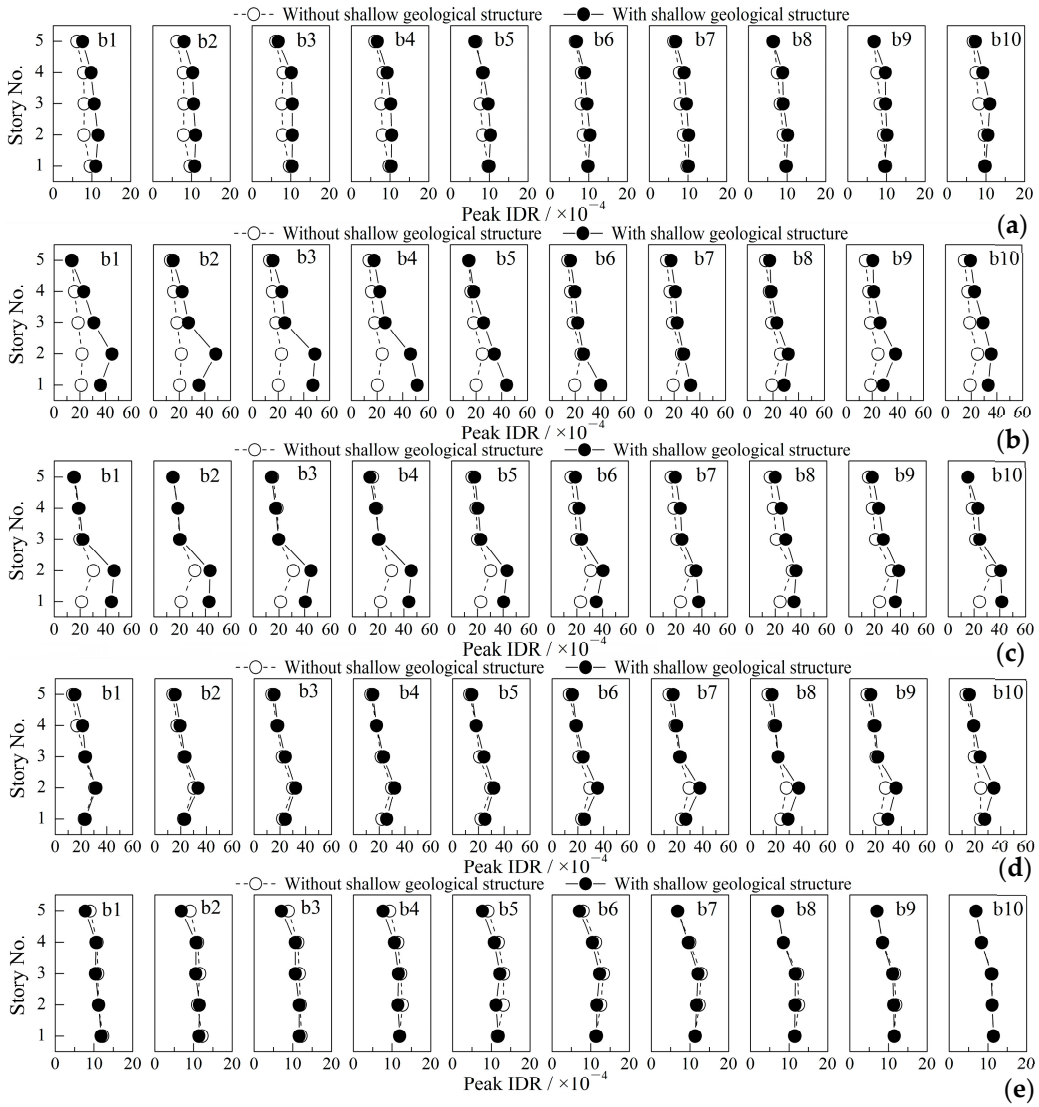


Figure 7. Comparison of peak IDRs of each structure in five building clusters, c1 (**a**), c2 (**b**), c3 (**c**), c4 (**d**), and c5 (**e**) for the two cases with and without the shallow geological structures.

Overall, the seismic responses of near-fault building clusters located at different positions are significantly different. Regardless of whether the influence of shallow geological structures is considered, building clusters c2–c4 in the rupture-forward area within ~1.5 km of the fault trace exhibit relatively large seismic responses and all enter the elastoplastic stage, which could be due to rupture-forward effect of reverse fault, while building clusters c1 and c5 at other positions have relatively small seismic responses and remain in the elastic stage; the positions where the maximum peak IDRs of structures with elastoplastic deformation occur are mainly concentrated on the first or second floor. It can also be seen from Figure 7 that the existence of shallow geological structures may change the position where the maximum peak IDR occurs, such as structures b4–b7 in building cluster c2.

To further quantitatively analyze the influence of shallow geological structures on the seismic response of building clusters, Figure 8 shows a comparison of the max peak IDRs of each structure in all building clusters under two scenarios: with and without considering shallow geological structures. Simultaneously, the figure also illustrates the damage degree of each structure in accordance with the China Code for Seismic Design

of Buildings (GB 50011-2010) [54], which specifies that the IDR can be used for evaluating structural damage degree. For R/C frame structures: an IDR < 1/550 indicates basic integrity; an IDR of 1/550–1/250 suggests slight damage; and an IDR of 1/250–1/120 implies moderate damage.

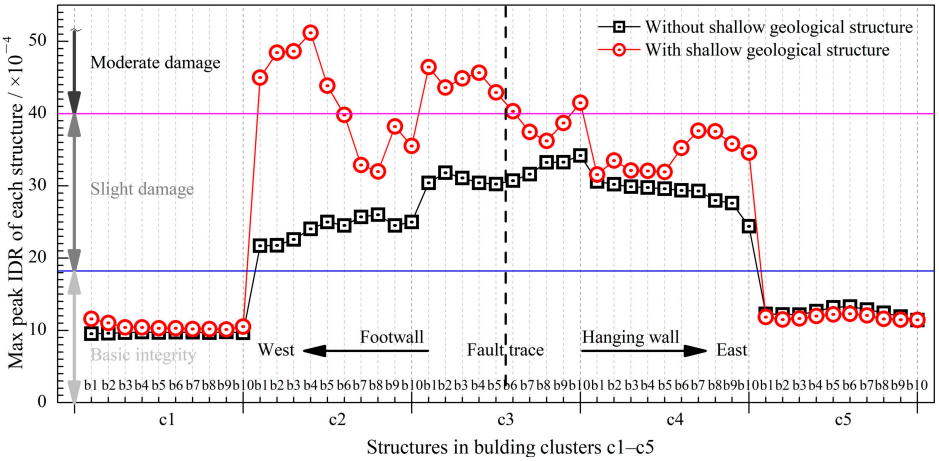


Figure 8. Comparison of max peak IDRs of each structure in building clusters c1–c5 for two cases, without and with shallow geological structures.

In general, for the case without shallow geological structures, the maximum peak IDR of one structure in the east of the fault trace is greater than that of the structure in the west of the fault trace with the same fault-trace distance as the eastern structure. In other words, these max peak IDRs exhibit the characteristics of the hanging-wall/footwall effects. However, for the case with shallow geological structures, these hanging-wall/footwall effects for the max peak IDRs are not observed. It means that the existence of the shallow geological structures may locally change hanging-wall/footwall effects for seismic response of near-fault building clusters.

For building cluster c1, the increased percentage in the max peak IDR of each structure caused by the shallow geological structure ranges from 3.50% to 21.55%; all the structures remain in the elastic stage and basic integrity. For building cluster c2, the corresponding increase percentage ranges from 22.95% to 122.91%, all the structures remain in the elasto-plastic stage, and the structures b1–b5 have progressed from slight damage to moderate damage. For building cluster c3, the corresponding increase percentage ranges from 8.94% to 52.68%, all the structures remain in the elastoplastic stage, and the structures b1–b6 and b10 have progressed from slight damage to moderate damage. For building cluster c4, the corresponding increase percentage ranges from 3.15% to 41.76%; all the structures remain in the elastoplastic stage, with slight damage. For building cluster c5, the corresponding increase percentage ranges from −7.46% to 0.14%; all the structures remain in the elastic stage and basic integrity.

Among these five building clusters, the seismic responses of building cluster c5, located outside the ground region of shallow geological structures, are slightly affected by them. Whereas the seismic responses of building clusters c1–c4 within this region are significantly affected to different extents: the seismic response of building cluster c2 at the surface of distinct LVZ M1 is most pronouncedly increased by shallow geological structures (max increase percentage: 122.91%); that of building cluster c3 on the surface of LVZ M2 is the next most increased (max increase percentage: 52.68%), followed by building cluster c4 on the ground of HVZ M4 (max increase percentage: 41.76%), and building cluster c1 at the surface of HVZ M3 is minimally impacted (max increase percentage: 21.55%). Naturally, the seismic responses of individual structures within each building cluster are affected by

shallow geological structures to varying degrees (e.g., structures b1–b10 in building cluster c4), which may be related to factors such as the shape and depth of the interfaces within the heterogeneous media beneath the buildings, as well as the reflection of seismic waves.

It is shown that the existence of LVZs may significantly amplify the seismic response of structures located on their ground surface and cause more severe structural damage, whereas the existence of HVZs may increase the seismic response of structures on their ground surface to a relatively lesser extent compared with the case of LVZs.

4.2.2. The Influence of the Shallow Geological Structure on Near-Fault Ground Motion

To study the influence of the shallow geological structure on ground motion, the horizontal PGAs are calculated at the 21 ground receivers P1–P21 with 400 m equidistant intervals in the range of fault-trace distance of 4.0 km for the two cases with and without shallow geological structures. For the case with shallow geological structures, as shown near the horizontal axis in Figure 9, receivers P1–P3 are located on M3's surface (P1: ~540 m from its western edge); P4–P6 on western M2's surface (P4: ~150 m from its western edge); P7–P10 on M1's surface (P7: ~300 m from its western edge); P11–P12 on eastern M2's surface (P11: ~150 m from its western edge); P13–P18 on M4's surface (P13: ~350 m from its western edge); and P19–P21 on eastern M5's surface (P19: ~200 m from M4's eastern edge).

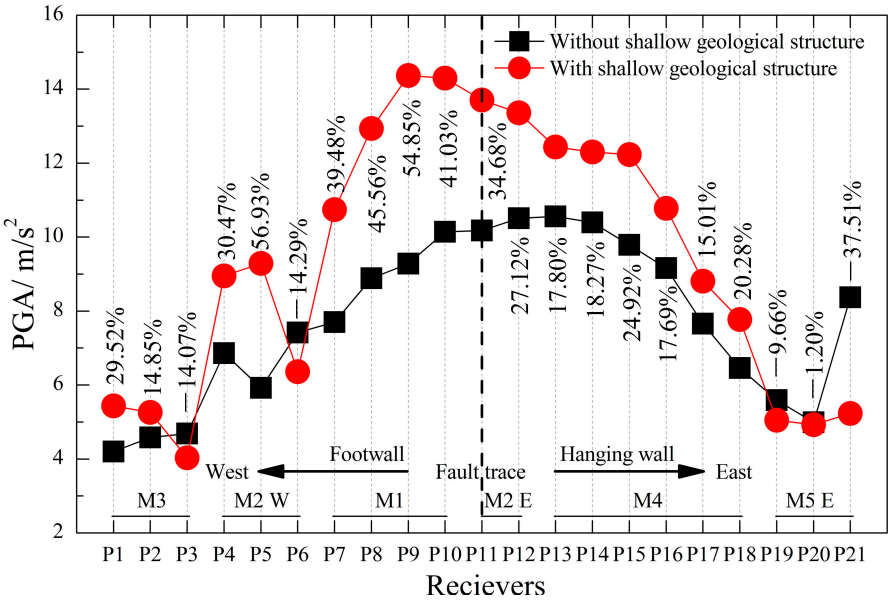


Figure 9. Comparison of the horizontal PGAs at receivers P1–P21, distributed equally with a 400 m interval, for two cases with and without shallow geological structures. The percentages represent the increase in percentage in PGAs at the corresponding receivers with shallow geological structures compared to the case without shallow geological structures. M1/M3/M4: the ground surface region of M1/M3/M4. M2 W: the ground surface region of the western part of M2. M2 E/M5 E: the ground surface region of the eastern part of M2/M5.

Figure 9 shows a comparison of the horizontal PGAs with and without shallow geological structures. Overall, whether or not shallow geological structures are considered, the PGA values at the receivers (P7–P15) within the 1.6 km fault-trace distance in rupture forward are significantly higher than those at other receivers. For the case without shallow geological structures, the horizontal PGAs at most of the receivers (excluding P18) on hanging wall are greater than ones (excluding P4) on footwall with equal fault-trace distance to the corresponding hanging-wall receivers; that is to say, most PGA values exhibit the characteristic of hanging-wall/footwall effect, but this effect is not very significant, this may be due to large fault dip angle. For the cases with shallow geological structures, the PGA

values do not have the characteristic of the hanging-wall/footwall effect. This means that the presence of shallow geological structures has locally changed the effect of PGA values.

Compared to the case without shallow geological structures, the increased percentages of PGA values for the case with shallow geological structures are −37.5% (P21) and–56.9% (P5). The increased percentages of the PGAs at most receivers (excluding P2) situated on the surface of HVZs M3 and M4 are below 25.0%. The increased percentages of the PGAs at most receivers (excluding P5) situated on the surface of LVZs M1 and M2 exceed 25.0%. This indicates that the amplification effect of LVZs on PGA values is overall significantly stronger than that of HVZs.

4.2.3. The Influence of Structural Nonlinearity on Seismic Responses of Near-Fault Building Clusters

To investigate the influence of structural nonlinearity on the seismic response of near-fault building clusters, using the computational model with shallow geological structures, two cases for linearly elastic and elastoplastic structures are considered to compare their structural seismic responses. Figure 10 shows a comparison of the first-floor inter-story drift time-history curves for structure b1 in each building cluster, accounting for elastic and elastoplastic structures.

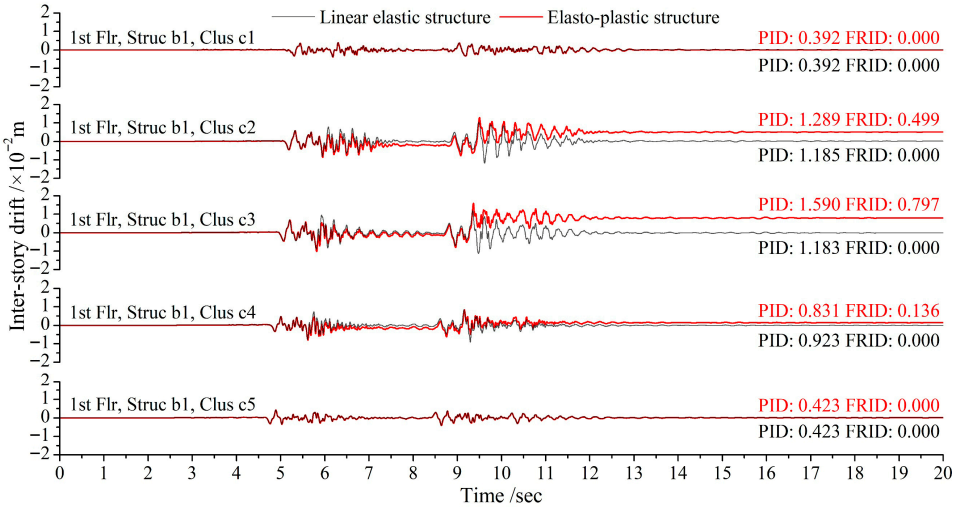


Figure 10. Comparison of the first-floor inter-story drifts of each structure b1 in building clusters c1-c5 between elastic and elastoplastic structures. PID: peak inter-story drift. FRID: final residual inter-story drift. The unit of PIDs and FRIDs is the same as that of the vertical axis.

For each structure b1 in both building clusters c1 and c5, the inter-story drift time-history curves are identical for both elastic and elastoplastic structures. This is mainly because each elastoplastic structure b1 in these two clusters still behaves elastically, as shown in Figure 8. For each structure b1 in three building clusters c2–c4, the first-floor inter-story drift time-history curve for an elastoplastic structure is different from that for an elastic structure. This is mainly because each elastoplastic structure b1 in these three clusters has entered the elastoplastic stage. Among those three clusters, c2–c4, the PID of each structure b1 in clusters c2 and c3 for the elastoplastic case is larger than that for the elastic case, whereas the PID of structure b1 in clusters c4 for the elastoplastic case is less than that for the elastic case. On the one hand, the structural elastoplastic behavior significantly produces an amplification effect on inter-story drift, which is caused by structural damage. On the other hand, the structural elastoplasticity has the energy-dissipating "seismic mitigation" effect on inter-story drift. When the amplification effect dominates, the PID for the elastoplastic case could be greater than that for the elastic case. When the energy-dissipating "seismic mitigation" effect dominates, the PID for the

elastoplastic case could be less than that for the elastic case. None of these phenomena can be captured by elastic-model-based structural seismic response analyses.

In clusters c2–c4, the elastic structures' first-floor FRIDs are equal to zero (i.e., no permanent deformation), but the elastoplastic structures have non-zero first-floor FRIDs (e.g., 0.499×10^{-2} m for structure b1 in cluster c2). It is shown that structural elastoplastic deformation could directly result in a non-zero FRID, yet this key damage feature cannot be reflected by the structural linear-elastic hypothesis.

To study near-fault seismic response characteristics of building clusters with structural nonlinearity, a comparative analysis is conducted on the horizontal motion displacements at the first-floor ground and the second-floor slab of structure b1 in building cluster c2 using structure models with linear elastic and elastoplastic deformations, as illustrated in Figures 11a and 11b, respectively. The following engineering demand parameters are studied for near-fault structural seismic response and ground motion: (1) permanent structural motion displacement (PSMD), is defined as the displacement relative to the initial undeformed equilibrium position of the structure; (2) permanent ground motion displacement (PGMD), which is the unrecoverable permanent displacement of the ground after earthquake excitation, relative to its initial position before the ground motion; final structural residual displacement (FSRD), which refers to the permanent, irrecoverable displacement of the superstructure after ground motion excitation, measured relative to one of its own initial equilibrium positions (e.g., the ground floor slab of the structure).

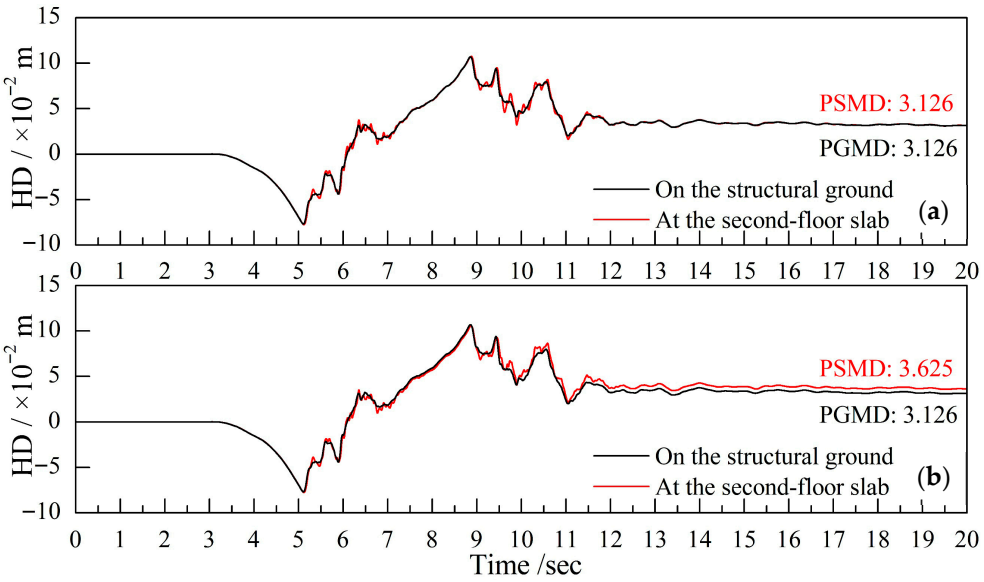


Figure 11. Comparison of ground and second-floor slab horizontal displacements considering structural elastic deformation (**a**) and elastoplastic deformation (**b**) for building b1 in building cluster c2. HD: horizontal displacement. The unit of PSMDs and PGMDs is the same as that of the vertical axis.

For the elastic structure shown in Figure 11a, PSMD at the second-floor slab is identical with PGMD because the near-fault elastic structure has no non-zero FSRD relative to the ground. For the elastoplastic-deforming structure shown in Figure 11b, the PSMD at the second-floor slab is 3.625×10^{-2} m and the corresponding near-fault PGMD is 3.126×10^{-2} m. That is to say, the PSMD at the second-floor slab exceeds the corresponding PGMD by 0.499×10^{-2} m, which is FSRD relative to the supporting ground (for the second-floor slab, it is just equal to the first-floor FRID shown in Figure 10). This implies that the PSMD for the near-fault structure undergoing elastoplastic deformation includes both non-zero PGMD and non-zero FSRD relative to the ground.

Although the above conclusions are derived from the elastoplastic-deforming multi-story structures near fault, these characteristics of ground motion effects on structures, PSMD, PGMD, FSRD, and their relationship, remain qualitatively valid for the elastoplastic-deforming high-rise buildings. Only their distribution and magnitude require quantitative adjustment according to structural dynamic properties.

The observed structure and ground seismic response characteristics mentioned above are dominated by two key mechanisms. First, the near-fault rupture directivity and permanent ground displacement provide a strong long-period impulse input, which causes significant inelastic deformation and large residual displacement in the structural system. Second, the shallow low-velocity geological structure traps and amplifies seismic waves, leading to enhanced ground-motion intensity and increased inter-story drift. The combined effect of these two factors is the fundamental reason for the distinct response distribution and the partially reversed hanging-wall/footwall effect observed in the simulations of structural seismic responses and ground motion.

5. Discussion

This study establishes an integrated numerical method for nonlinear seismic response analysis of near-fault building clusters, which couples the fault-rupture process, viscoelastic wave propagation, structural nonlinear seismic responses, and SCI. The method is verified by a shaking table test and then applied to Xichang City under a hypothetical M_w6.8 reverse earthquake within the Anninghe Fault. Results indicate that building clusters within ~1.5 km in the rupture-forward zone enter the elastoplastic state regardless of shallow geological structures, while those outside this region remain elastic. The maximum IDRs are mainly concentrated on the first and second floors. Shallow geological structures, especially LVZs, significantly amplify structural seismic responses and PGAs within these zones, potentially causing more severe damage to the overlying buildings and locally reversing conventional hanging-wall/footwall effects. For elastoplastic near-fault structures, the PSMD consists of both PGMD and FSRD with respect to the supporting ground.

5.1. Engineering Implications

The reversal of hanging-wall/footwall effects induced by shallow geological structures demonstrates that traditional seismic hazard zoning, which relies solely on fault location, is inadequate for near-fault regions. Local geological conditions, particularly the distribution of low-velocity and high-velocity zones, should be fully incorporated into seismic risk evaluation. Buildings situated above low-velocity zones usually experience amplified seismic responses and more severe damage, and thus need higher seismic fortification levels. The observation that maximum inter-story drift ratios are mainly concentrated on the first and second floors implies that the seismic performance of lower stories should be emphatically improved in the seismic design of near-fault buildings. In addition, the permanent displacement mechanism (PSMD = PGMD + FSRD relative to the supporting ground) offers an important theoretical basis for post-earthquake damage assessment, structural rehabilitation, and urban seismic resilience evaluation. The proposed method can provide a valuable reference for scientific site selection, seismic design optimization, and disaster-prevention planning of building clusters in near-fault mountainous cities.

5.2. Research Uncertainties

5.2.1. Structural Parameter Uncertainties

The structural parameters involved in this study have certain uncertainties, including the elastoplastic stiffness coefficient, the Rayleigh damping coefficients, and the elastic limit inter-story drift ratio. These parameters directly affect the judgment of the structural

elastoplastic state, the evolution of hysteretic behavior, and the calculation results of inter-story drift and residual displacement.

To mitigate the uncertainty of structural parameters, systematic parameter sensitivity analysis should be carried out to clarify the influence weight of each parameter on nonlinear seismic responses. Meanwhile, parameters should be calibrated based on experimental data and code-suggested values as much as possible, and reasonable value ranges should be determined to ensure the rationality of structural modeling.

In the present study, all parameters are determined strictly according to the current seismic design code and commonly adopted values in the literature [55–57], which ensures the rationality of parameter selection. For the sensitivity of the structural response to the post-yield stiffness ratio for a 5-story structure, referring to Figure 8a in the literature [71], the ductility factor (i.e., $\Delta u_{l,\max}/\Delta u_l^e$) shows a weak sensitivity to the post-yield stiffness ratio of 0.05–0.1, with maximum relative deviation (the 4th story) up to ~14.5% in all stories.

5.2.2. Geomedia Parameter Uncertainties

The geomedia parameters with uncertainties mainly include *P*-wave/*S*-wave quality factors, wave velocities, mass density, the geometric dimensions, and material distribution of LVZs and HVZs. These parameters control the propagation and attenuation of seismic waves as well as the amplification effects of shallow geological structures, thereby directly affecting ground-motion characteristics and structural input excitations.

Parameter sensitivity analysis is particularly critical for identifying key influential parameters and quantifying their impacts on numerical results. To reduce the uncertainty of geomedia parameters, high-resolution field surveys and geophysical detection data should be adopted to optimize the geological model. Meanwhile, parameter sensitivity analysis and interval analysis can be jointly used to evaluate the influence of parameter fluctuations on simulation results, so as to verify the robustness and reliability of key conclusions.

In this study, geomedia parameters are taken from high-resolution field surveys and geophysical data in published literature [34,67,68]. Systematic sensitivity analysis is not conducted here, but will be included in future work to verify the robustness of the results.

5.2.3. Fault Source Parameter Uncertainties

The kinematic fault model adopted in this study involves uncertain parameters such as fault slip displacement, rise time, and rupture velocity. Although this model can effectively characterize rupture directivity and permanent ground displacement, it differs from the dynamic fault model in describing complete fault dynamic behavior, which could bring mild uncertainty to ground motion simulation.

To improve the reliability of fault-related simulations, parameters could be further referenced from typical geological and seismological results of the Anninghe Fault Zone.

In this study, all fault parameters are determined by using empirical formulas from global fault earthquake statistics [33,65,69,70]. In future work, comparisons between kinematic and dynamic fault models will be conducted to further clarify their applicable ranges.

5.3. Research Limitations and Future Work

This study adopts a two-dimensional plane-strain assumption, which may not fully represent three-dimensional dynamic interactions between soil and building clusters. Future research may gradually introduce three-dimensional modeling for more comprehensive analysis.

The building clusters are simplified as identical regular 5-story RC frames, which differ from real urban buildings with varied heights, irregular plans, and mixed structural systems. These real urban building clusters may lead to rocking or torsional responses, inconsistent dynamic characteristics, and uneven deformations [15–18]. These effects can

change the amplitude and distribution of structural seismic responses, thereby affecting the applicability of the conclusions. More realistic building configurations could be considered in future work to improve simulation fidelity.

Only one earthquake scenario (M_w6.8 reverse fault) is discussed in this study. For broader applicability, the same research thinking and approach may be extended to other fault mechanisms, earthquake magnitudes, and geological conditions in subsequent studies.

In addition, the adopted bilinear hysteretic model captures the dominant nonlinear behavior but does not consider stiffness degradation, strength deterioration, or cyclic cumulative damage. These effects could be integrated into advanced constitutive models in future studies to better characterize structural nonlinearity.

Nevertheless, we emphasize that despite the above limitations, the proposed model is reasonable and efficient for revealing the global seismic response patterns of building clusters under near-fault ground motions. Within the scope of the adopted assumptions, the core findings regarding displacement characteristics, dynamic amplification effects, and inter-story response trends remain robust.

6. Conclusions

A new type of integrated numerical method is developed to obtain the nonlinear seismic response of near-fault building clusters due to the fault rupture by considering structural elastoplastic deformation. A numerical example is performed to verify the validity and correctness in dealing with dynamic SCI by comparing the numerical results of the developed method with the results of a table shaking test. By using the developed method, the near-fault structural seismic response and ground motion at different mountainous locations in Xichang City are simulated during an M_w6.8 hypothetical earthquake in the Anninghe Fault Zone. This study focuses on three influences: shallow geological structures affecting the seismic response of near-fault building clusters; shallow geological structures affecting near-fault ground motion; and structural nonlinearity affecting the seismic response of near-fault building clusters. The main conclusions are as follows:

(1) Dominated by the rupture-forward effect, the building clusters in the rupture-forward area within the fault-trace distance of ~1.5 km exhibit significant seismic responses and enter the elastoplastic stage regardless of shallow geological structure influences, while the clusters outside this area remain elastic with minor responses. This reveals that the rupture-forward effect is a key contributor to the seismic vulnerability of near-fault building clusters.

(2) The maximum peak IDRs of elastoplastically deformed structures are mainly concentrated on the first or second floor, providing direct guidance for the seismic design and retrofitting prioritization of near-fault building clusters.

(3) The existence of shallow geological structures may locally reverse the hanging-wall/footwall effects of the seismic response of near-fault building clusters and ground motion.

(4) The existence of LVZs significantly amplifies the seismic response of their superstructures, which may result in more severe structural damage, while the amplification effect of HVZs on their surface structures is notably weaker than that of LVZs. The amplification effect of LVZs on their surface PGA values is generally significantly stronger than that of HVZs.

(5) For near-fault structures with elastoplastic deformation, the PSMD at the slab of a specific floor comprises both non-zero PGMD and non-zero FSRD relative to the ground.

This study provides an effective numerical analysis tool for nonlinear seismic responses of near-fault building clusters by considering structural elastoplastic behavior. It

could contribute to seismic damage assessment, site selection, and structural optimization design of near-fault building clusters.

Author Contributions: Conceptualization, W.Z. and T.L.; Methodology, W.Z. and T.L.; Software, W.Z.; Validation, W.Z.; Investigation, W.Z., T.L. and Z.Z.; Resources, B.Q.; Data Curation, P.Y.; Writing—Original Draft Preparation, W.Z.; Writing—Review and Editing, W.Z., T.L. and B.Q.; Visualization, P.Y.; Supervision, W.Z.; Funding Acquisition, W.Z. and Z.Z. All authors have read and agreed to the published version of the manuscript.

Funding: This work was supported by the National Natural Science Foundation of China [Grant No. 52278513], Xichang Science and Technology Program [Grant No. JSYJ-2024-03] and Scientific and Technological Research Program of Xichang University [Grant No. CM2025013].

Data Availability Statement: The data are available from the corresponding author upon reasonable request.

Conflicts of Interest: The authors declare no conflicts of interest.

Nomenclatures and Abbreviations

Symbols	Meaning
L	Total number of building stories
l	The lth inter-story segment, $l = 1,\ldots,L$
$\mathrm{f}_l/\mathrm{f}_{l+1}$	Lower/upper endpoint of the lth segment
Cf_{l+1}	Centroid of structural investigated lump f_{l+1}
u_{f_1}	Horizontal displacement at the point f_1 of connecting investigated lump f_1
w_{f_1}	Vertical displacement at the point f_1 of connecting investigated lump f_1
θ_{f_1}	Angular displacement at the point f_1 of connecting investigated lump f_1
$u_{\mathrm{f}_{l+1}}$	Horizontal displacement at the point f_{l+1} of structural investigated lump f_{l+1}
$w_{\mathrm{f}_{l+1}}$	Vertical displacement at the point f_{l+1} of structural investigated lump f_{l+1}
$\theta_{\mathrm{f}_{l+1}}$	Angular displacement at the point f_{l+1} of structural investigated lump f_{l+1}
$u_{\mathrm{Cf}_{l+1}}$	Horizontal displacement at the centroid Cf_{l+1} of structural investigated lump f_{l+1}
$w_{\mathrm{Cf}_{l+1}}$	Vertical displacement at the centroid Cf_{l+1} of structural investigated lump f_{l+1}
$\theta_{\mathrm{Cf}_{l+1}}$	Angular displacement at the centroid Cf_{l+1} of structural investigated lump f_{l+1}
$(EA)_l$	Equivalent axial stiffness of the lth segment
$(EI)_l$	Equivalent bending stiffness of the lth segment
$(GA_s)_l$	Equivalent shear stiffness of the lth segment
V_l	Shear force acting on the mid-section of the lth segment
N_l	Axial force acting on the mid-section of the lth segment
M_l	Bending moment acting on the mid-section of the lth segment
β_1	Mass damping coefficient for Rayleigh damping
β_2	Stiffness damping coefficient for Rayleigh damping
ω_i	ith circular natural frequency (subscript i denotes the mode order)
ζ_i	ith modal damping ratio (subscript i denotes the mode order)
SSI	Site-structure interaction
SSSI	Structure-site-structure interaction
SCI	Site-city interaction
GZB	Generalized Zener body
RMSE	Root mean square error
LVZ	Low-velocity zone
HVZ	High-velocity zone
IDR	Inter-story drift ratio
PGA	Peak ground acceleration
PID	Peak inter-story drift
FRID	Final residual inter-story drift
PSMD	Permanent structural motion displacement

PDMD	Permanent ground motion displacement
FSRD	Final structural residual displacement

Appendix A

Following the research work [72], the original *P*- and *S*-wave relaxation functions, Equation (A5) in Robertsson et al. (1994) [73] and Equation (25) in Jousset et al. (2004) [74], omitted the term $1/L$ before the summation symbol. In this Appendix, the *P*- and *S*-wave relaxation function-based GZB viscoelastic constitutive equation with memory variables is re-derived after rectifying the omission of $1/L$ (which is replaced by $1/N$ hereinafter). In comparison with our previous studies [33,34], on the one hand, this type of viscoelastic constitutive equation permits us to define Q_P and Q_S independently; on the other hand, it enables the direct derivation of the parameters for *P*-waves and *S*-waves, as well as the relaxation frequencies from the constants Q_P and Q_S.

For a linear viscoelastic material, the relationship between the stress-tensor components σ_{ij} and the strain-tensor components ε_{kl} is [75]

$$\sigma_{ij} = G_{ijkl} * \dot{\varepsilon}_{kl} = \dot{G}_{ijkl} * \varepsilon_{kl} \tag{A1}$$

where the dot above the variable represents a derivative with respect to time and $*$ the time convolution. The G_{ijkl} is a component form of a fourth-order tensor **G** which is called the relaxation function.

For an isotropic homogeneous material, **G** collapses into two independent functions: the relaxation function Λ (analogous to the first Lamé constant λ in the elastic case) and the shear relaxation function M (analogous to the second Lamé constant or the shear modulus μ in an elastic case). The component form of the isotropic fourth-order tensor **G** is given by [75]

$$G_{ijkl} = \Lambda\delta_{ij}\delta_{kl} + M(\delta_{ik}\delta_{jl} + \delta_{il}\delta_{jk}) \tag{A2}$$

where δ_{ij} is the Kronecker delta.

Substituting $\Lambda = \Pi - 2M$ [74] into Equation (A2), and taking a time derivative of G_{ijkl}, the following equation is obtained

$$\dot{G}_{ijkl} = (\dot{\Pi} - 2\dot{M})\delta_{ij}\delta_{kl} + \dot{M}(\delta_{ik}\delta_{jl} + \delta_{il}\delta_{jk}) \tag{A3}$$

where Π is the tension-compression relaxation function, which is analogous to $\lambda + 2\mu$ in an elastic case.

Substituting (A3) into (A1) gives

$$\sigma_{ij} = (\dot{\Pi} - 2\dot{M})\delta_{ij} * \varepsilon_{kk} + 2\dot{M} * \varepsilon_{ij} \tag{A4}$$

In this study, the GZB (also named as the general standard linear solid with *N* mechanisms) is used for representing viscoelastic characteristics of the material. The tension-compression relaxation function Π and shear relaxation function M are respectively expressed as

$$\Pi = \pi^R(1 + \frac{1}{N}\sum_{n=1}^{N}\chi_{Pn}e^{-\omega_n t})H(t) \tag{A5}$$

$$M = \mu^R(1 + \frac{1}{N}\sum_{n=1}^{N}\chi_{Sn}e^{-\omega_n t})H(t) \tag{A6}$$

where χ_{Pn} is the viscoelastic parameter for *P* wave and $\chi_{Pn} = \tau_{\varepsilon n}^P/\tau_{\sigma n} - 1$, χ_{Sn} is the viscoelastic parameter for *S* wave and $\chi_{Sn} = \tau_{\varepsilon n}^S/\tau_{\sigma n} - 1$, ω_n is the stress relaxation frequency and $\omega_n = 1/\tau_{\sigma n}$. The $\tau_{\varepsilon n}^P$ and $\tau_{\varepsilon n}^S$ are respectively strain relaxation times for *P* wave and *S* wave. The $\tau_{\sigma n}$ is the stress relaxation time. The π^R and μ^R are the relaxed

modulus (elastic modulus, $\pi^R = \lambda + 2\mu$, $\mu^R = \mu$). $H(t)$ is Heaviside function. The introduction of the relaxation Π allows us to define Q_P and Q_S independently through the parameters χ_{Pn} (P-waves) and χ_{Sn} (S-waves).

Using the time derivative of the relaxation functions Π and M, we can obtain

$$\dot{\Pi} = \pi^R(1 + \frac{1}{N}\sum_{n=1}^{N}\chi_{Pn}e^{-\omega_n t})\delta(t) - \pi^R\frac{1}{N}\sum_{n=1}^{N}\omega_n\chi_{Pn}e^{-\omega_n t}H(t) \tag{A7}$$

$$\dot{M} = \mu^R(1 + \frac{1}{N}\sum_{n=1}^{N}\chi_{Sn}e^{-\omega_n t})\delta(t) - \mu^R\frac{1}{N}\sum_{n=1}^{N}\omega_n\chi_{Sn}e^{-\omega_n t}H(t) \tag{A8}$$

where $\delta(t)$ is Dirac delta function.

Substituting $\dot{\Pi}$ and $\dot{M}$ into Equation (A4), we can give the following expressions

$$\sigma_{ij} = (\pi^U - 2\mu^U)\delta_{ij}\varepsilon_{kk} + 2\mu^U\varepsilon_{ij} + \frac{1}{N}\sum_{n=1}^{N}R_{ijn} \tag{A9}$$

$$R_{ijn} = -\omega_n(\pi^R\chi_{Pn}e^{-\omega_n t} - 2\mu^R\chi_{Sn}e^{-\omega_n t})H(t)\delta_{ij} * \varepsilon_{kk} - 2\mu^R\omega_n\chi_{Sn}e^{-\omega_n t}H(t) * \varepsilon_{ij} \tag{A10}$$

where the R_{ijn} is named as memory variable. The π^U and μ^U are the unrelaxed modulus. They are given as follows

$$\pi^U = \pi^R(1 + \frac{1}{N}\sum_{n=1}^{N}\chi_{Pn}), \mu^U = \mu^R(1 + \frac{1}{N}\sum_{n=1}^{N}\chi_{Sn}) \tag{A11}$$

Taking a time derivative of the memory viable, we can obtain

$$\dot{R}_{ijn} = -\omega_n R_{ijn} - \omega_n(\pi^R\chi_{Pn} - 2\mu^R\chi_{Sn})\delta_{ij}\varepsilon_{kk} - 2\mu^R\omega_n\chi_{Sn}\varepsilon_{ij} \tag{A12}$$

in the Equations (A9), (A10) and (A12), for the 3-D problem, $i, j, k = x, y, z$; for the plane strain problem in coordinate system xoz in this study, $i, j, k = x, z$.

According to Equations (A9) and (A12) and rearranging them, the GZB viscoelastic constitutive equations with memory variables for the plane strain problem are written as follows

$$\sigma_{xx} = \pi^U(\frac{\partial u}{\partial x} + \frac{\partial w}{\partial z}) - 2\mu^U\frac{\partial w}{\partial z} + \frac{1}{N}\sum_{n=1}^{N}R_{xxn} \tag{A13}$$

$$\sigma_{zz} = \pi^U(\frac{\partial u}{\partial x} + \frac{\partial w}{\partial z}) - 2\mu^U\frac{\partial u}{\partial x} + \frac{1}{N}\sum_{n=1}^{N}R_{zzn} \tag{A14}$$

$$\sigma_{xz} = \mu^U(\frac{\partial u}{\partial z} + \frac{\partial w}{\partial x}) + \frac{1}{N}\sum_{n=1}^{N}R_{xzn} \tag{A15}$$

$$\dot{R}_{xxn} = -\omega_n R_{xxn} - \pi^R\omega_n\chi_{Pn}(\frac{\partial u}{\partial x} + \frac{\partial w}{\partial z}) + 2\mu^R\omega_n\chi_{Sn}\frac{\partial w}{\partial z} \tag{A16}$$

$$\dot{R}_{zzn} = -\omega_n R_{zzn} - \pi^R\omega_n\chi_{Pn}(\frac{\partial u}{\partial x} + \frac{\partial w}{\partial z}) + 2\mu^R\omega_n\chi_{Sn}\frac{\partial u}{\partial x} \tag{A17}$$

$$\dot{R}_{xzn} = -\omega_n R_{xzn} - \mu^R\omega_n\chi_{Sn}(\frac{\partial u}{\partial z} + \frac{\partial w}{\partial x}) \tag{A18}$$

Using backward difference method, the stress components σ_{xx}, σ_{zz} and σ_{xz} at time $t + \Delta t$ can be obtained as follows

$$\sigma_{xx}^{t+\Delta t} = \pi^U[(\frac{\partial u}{\partial x})^{t+\Delta t} + (\frac{\partial w}{\partial z})^{t+\Delta t}] - 2\mu^U(\frac{\partial w}{\partial z})^{t+\Delta t} + \frac{1}{N}\sum_{n=1}^{N}R_{xxn}^{t+\Delta t} \tag{A19}$$

$$\sigma_{zz}^{t+\Delta t} = \pi^U[(\frac{\partial u}{\partial x})^{t+\Delta t} + (\frac{\partial w}{\partial z})^{t+\Delta t}] - 2\mu^U(\frac{\partial u}{\partial x})^{t+\Delta t} + \frac{1}{N}\sum_{n=1}^{N}R_{zzn}^{t+\Delta t} \tag{A20}$$

$$\sigma_{xz}^{t+\Delta t} = \mu^U[(\frac{\partial u}{\partial z})^{t+\Delta t} + (\frac{\partial w}{\partial x})^{t+\Delta t}] + \frac{1}{N}\sum_{n=1}^{N}R_{xzn}^{t+\Delta t} \tag{A21}$$

https://doi.org/10.3390/buildings16091769

$$R_{xxn}^{t+\Delta t} = c_n R_{xxn}^{t} - \pi^R \chi_{Pn} c_n \omega_n \Delta t[(\frac{\partial u}{\partial x})^{t+\Delta t} + (\frac{\partial w}{\partial z})^{t+\Delta t}] + 2\mu^R \chi_{Sn} c_n \omega_n \Delta t(\frac{\partial w}{\partial z})^{t+\Delta t} \quad \text{(A22)}$$

$$R_{zzn}^{t+\Delta t} = c_n R_{zzn}^{t} - \pi^R \chi_{Pn} c_n \omega_n \Delta t[(\frac{\partial u}{\partial x})^{t+\Delta t} + (\frac{\partial w}{\partial z})^{t+\Delta t}] + 2\mu^R \chi_{Sn} c_n \omega_n \Delta t(\frac{\partial u}{\partial x})^{t+\Delta t} \quad \text{(A23)}$$

$$R_{xzn}^{t+\Delta t} = c_n R_{xzn}^{t} - \mu^R \chi_{Sn} c_n \omega_n \Delta t[(\frac{\partial u}{\partial z})^{t+\Delta t} + (\frac{\partial w}{\partial x})^{t+\Delta t}] \quad \text{(A24)}$$

where $c_n = 1/(1 + \omega_n \Delta t)$. The spatial derivatives of displacement for the triangular grid can be obtained from the literature [61]. The parameters χ_{Pn} for *P*-waves and χ_{Sn} for *S*-waves as well as stress relaxation frequency ω_n can be evaluated directly from the known constant quality factors Q_P and Q_S through least squares technique [76].

References

1. Zhang, G.; Ji, Y.; Guo, H.; Hu, X. Complex fault geometry of the 1976 *Ms* 7.8 Tangshan earthquake source region in North China. *Tectonophysics* **2022**, *845*, 229642. [CrossRef]
2. Nishino, T.; Hada, A.; Kawase, H.; Matsushima, S. Empirical seismic fragility function for fire doors based on inspection data from the 1995 Kobe earthquake and its use in post-earthquake fire risk assessments. *J. Build. Eng.* **2025**, *104*, 112362. [CrossRef]
3. Cao, Z.; Wei, J.; Sun, Z.; Song, W. Spatial characteristic analysis of near-fault velocity pulses based on simulation of earthquake ground motion fields. *Buildings* **2025**, *15*, 1363. [CrossRef]
4. Demir, A. Post-earthquake structural damage assessment, lessons learned, and addressing objections following the 2023 Kahramanmaras, Turkey earthquakes. *Bull. Earthq. Eng.* **2025**, *23*, 1107–1127. [CrossRef]
5. Wirgin, A.; Bard, P.Y. Effects of buildings on the duration and amplitude of ground motion in Mexico City. *Bull. Seismol. Soc. Am.* **1996**, *86*, 914–920. [CrossRef]
6. Tsogka, C.; Wirgin, A. Simulation of seismic response in an idealized cit. *Soil Dyn. Earthq. Eng.* **2003**, *23*, 391–402. [CrossRef]
7. Groby, J.; Tsogka, C.; Wirgin, A. Simulation of seismic response in a city-like environment. *Soil Dyn. Earthq. Eng.* **2005**, *25*, 487–504. [CrossRef]
8. Groby, J.P.; Wirgin, A. Seismic motion in urban sites consisting of blocks in welded contact with a soft layer overlying a hard half-space. *Geophys. J. Int.* **2008**, *172*, 725–758. [CrossRef]
9. Kham, M.; Semblat, J.F.; Bard, P.Y.; Dangla, P. Seismic site-city interaction: Main governing phenomenon through simplified numerical models. *Bull. Seismol. Soc. Am.* **2006**, *96*, 1934–1951. [CrossRef]
10. Sahar, D.; Narayan, J.P.; Kumar, N. Study of role of basin shape in the site–city interaction effects on the ground motion characteristics. *Nat. Hazards* **2015**, *75*, 1167–1186. [CrossRef]
11. Kato, B.; Wang, G. Seismic site-city interaction analysis of super-tall buildings surrounding an underground station: A case study in Hong Kong. *Bull. Earthq. Eng.* **2022**, *20*, 1431–1454. [CrossRef]
12. Gueguen, P.; Bard, P.Y.; Semblat, J.F. Engineering seismology: Seismic hazard and risk analysis: Seismic hazard analysis from soil-structure to site-city interaction. In *12th World Conference on Earthquake Engineering, Auckland, New Zealand*; Paper 0555; International Association for Earthquake Engineering: Tokyo, Japan, 2000.
13. Chen, S.; Zhai, C.; Liu, Q.; Ji, D.; Wen, W.; Xie, L. Assessing the influence of nonlinear soil behaviour on site-city interaction. *Soil Dyn. Earthq. Eng.* **2023**, *171*, 107973. [CrossRef]
14. Wang, J.; Guo, T.; Xie, Y.; Du, Z. Parametric analyses of dynamic interaction between three-dimensional soil and frame structure group under earthquake loadings. *Bull. Earthq. Eng.* **2022**, *20*, 8305–8324. [CrossRef]
15. Norouzi, A.H.; Gerami, M.; Vahdani, R.; Sivandi-Pour, A. Influence of site–city interaction on the response of structures considering soil stiffness, height, and number of buildings. *Earthq. Eng. Struct. Dyn.* **2021**, *50*, 1290–1314. [CrossRef]
16. Lu, X.; Tian, Y.; Wang, G.; Huang, D. A numerical coupling scheme for nonlinear time history analysis of buildings on a regional scale considering site-city interaction effects. *Earthq. Eng. Struct. Dyn.* **2018**, *47*, 2708–2725.
17. Zhang, B.; Xiong, F.; Lu, Y.; Mei, Z.; Ran, M. Regional seismic damage analysis considering soil–structure cluster interaction using lumped parameter models: A case study of Sichuan University Wangjiang Campus buildings. *Bull. Earthq. Eng.* **2021**, *19*, 4289–4310. [CrossRef]
18. Tian, Y.; Lyu, S.H.; Xu, Z.; Wang, M.X. Regional seismic fragility analysis of building clusters considering site–city interactions. *Eng. Struct.* **2026**, *351*, 121996. [CrossRef]
19. Abrahamson, N.A.; Somerville, P.G. Effects of the hanging wall and footwall on ground motions recorded during the Northridge earthquake. *Bull. Seismol. Soc. Am.* **1996**, *86*, S93–S99. [CrossRef]
20. Somerville, P.G. Magnitude scaling of the near fault rupture directivity pulse. *Phys. Earth Planet. Inter.* **2003**, *137*, 201–212. [CrossRef]

21. Mavroeidis, G.P.; Papageorgiou, A.S. A mathematical representation of near-fault ground motions. *Bull. Seismol. Soc. Am.* **2003**, *93*, 1099–1131. [CrossRef]
22. Abrahamson, N.A. Effects of rupture directivity on probabilistic seismic hazard analysis. In Proceedings of the 6th International Conference on Seismic Zonation, Palm Springs, CA, USA, 12–15 November 2000; Volume 1, pp. 151–156.
23. Bray, J.D.; Rodriguez-Marek, A. Characterization of forward-directivity ground motions in the near-fault region. *Soil Dyn. Earthq. Eng.* **2004**, *24*, 815–828.
24. Wang, T.; Zhang, X.A.; Yang, S.; Shahzad, M.M. Quantifying the influence of modeling uncertainties on performance evaluation of mega column-core tube-outrigger structure under near-field and far-field ground motions. *J. Build. Eng.* **2022**, *59*, 105052. [CrossRef]
25. Fan, B.; Zhang, X.A.; Xiao, Y.; Abdulhadi, M.; Wang, X.; Shahzad, M.M. Failure mode and optimization for MSCSS with LRBs based on IDA method. *Buildings* **2022**, *12*, 998. [CrossRef]
26. Shahzad, M.M.; Zhang, X.A.; Wang, X.; Abdulhadi, M.; Xiao, Y.; Fan, B. Plastic deformation analysis of a new mega-subcontrolled structural system (MSCSS) subjected to seismic excitation. *Buildings* **2022**, *12*, 987. [CrossRef]
27. Fernandez, A.; Bielak, J. Interaction between earthquake ground motion and multiple buildings in urban regions. In *Proceedings of the 3rd UJNR Workshop on Soil-Structure Interaction, Menlo Park, CA, USA, 29–30 March 2004*; Celebi, M., Todorovska, M.I., Okawa, I., Iiba, M., Eds.; U.S. Geological Survey (USGS): Reston, VA, USA, 2004.
28. Taborda, R. *Three-Dimensional Nonlinear Soil and Site-City Effects in Urban Regions*; Carnegie Mellon University: Pittsburgh, PA, USA, 2010.
29. Taborda, R.; Bielak, J. Large-scale earthquake simulation: Computational seismology and complex engineering systems. *Comput. Sci. Eng.* **2011**, *13*, 14–26. [CrossRef]
30. Guidotti, R.; Mazzieri, I.; Stupazzini, M.; Dagna, P. 3D numerical simulation of the site-city interaction during the 22 February 2011 M_w 6.2 Christchurch earthquake. In Proceedings of the 15th World Conference of Earthquake Engineering, 15th WCEE, Lisbon, Portugal, 24–28 September 2012.
31. Isbiliroglu, Y. *Coupled Soil-Structure Interaction Effects of Symmetric and Asymmetric Buildings in Urban Regions*; Carnegie Mellon University: Pittsburgh, PA, USA, 2013.
32. Isbiliroglu, Y.; Taborda, R.; Bielak, J. Coupled soil-structure interaction effects of building clusters during earthquakes. *Earthq. Spectra* **2015**, *31*, 463–500.
33. Liu, T.; Luan, Y.; Zhong, W. Earthquake responses of clusters of building structures caused by a near-field thrust fault. *Soil Dyn. Earthq. Eng.* **2012**, *42*, 56–70.
34. Liu, T.; Zhong, W. Earthquake responses of near-fault frame structure clusters due to thrust fault by using flexural wave method and viscoelastic model of earth medium. *Soil Dyn. Earthq. Eng.* **2014**, *61–62*, 57–62. [CrossRef]
35. Liu, T.; Zhong, W. Earthquake responses of near-fault building clusters in mountain city considering viscoelasticity of earth medium and process of fault rupture. *Soil Dyn. Earthq. Eng.* **2017**, *99*, 137–141. [CrossRef]
36. Zhong, W.; Liu, T.; Jiang, Y.; Qian, B. Seismic responses of near-fault building clusters including in-plane rotational component in investigated lump model of earth medium. *Soil Dyn. Earthq. Eng.* **2023**, *167*, 107796.
37. Öztürk, M.; Karan, M.A. Impact of near-fault seismic inputs on building performance: A case study informed by the 2023 Maras earthquakes. *Buildings* **2025**, *15*, 10142. [CrossRef]
38. Kenawy, M.; Pitarka, A. Performance assessment of near-fault buildings subjected to physics-based simulated earthquake ground motions with fling step. *Soil Dyn. Earthq. Eng.* **2025**, *166*, 107865. [CrossRef]
39. Ma, X.; Liu, Z.; Xiao, X. Seismic fragility analysis of a multi-tower super high-rise building under near-fault ground motions. *J. Earthq. Eng.* **2024**, *28*, 7614–7634. [CrossRef]
40. Nuti, C.; Briseghella, B.; Lavorato, D.; Taciroglu, E.; Bergami, A.V. Effects of near-fault ground motions on civil infrastructure. *Appl. Sci.* **2023**, *13*, 5929. [CrossRef]
41. Mazza, M. Effects of near-fault ground motions on the nonlinear behaviour of reinforced concrete framed buildings. *Earthq. Sci.* **2015**, *28*, 285–302. [CrossRef]
42. Liang, J.; Fu, J.; Todorovska, M.I.; Trifunac, M.D. Effects of the site dynamic characteristics on soil–structure interaction (I): Incident SH-Waves. *Soil Dyn. Earthq. Eng.* **2013**, *44*, 27–37. [CrossRef]
43. Firoj, M.; Bahuguna, A.; Kanth, A.; Agrahari, R. Effect of nonlinear soil−structure interaction and lateral stiffness on seismic performance of mid− rise RC building. *J. Build. Eng.* **2022**, *59*, 105096. [CrossRef]
44. Poudel, N.; Chaulagain, H. Numerical investigation of nonlinear soil-structure interaction effects on response of irregular RC buildings. *Results Eng.* **2024**, *22*, 102161. [CrossRef]
45. Han, B.; Chen, S.; Liang, J. 2D dynamic structure-soil-structure interaction: A case study of Millikan Library Building. *Eng. Anal. Bound. Elem.* **2020**, *113*, 346–358. [CrossRef]

46. Aldaikh, H.; Alexander, N.A.; Ibraim, E.; Oddbjornsson, O. Two dimensional numerical and experimental models for the study of structure–soil–structure interaction involving three buildings. *Comput. Struct.* **2015**, *150*, 79–91. [CrossRef]
47. Madani, B.; Behnamfar, F.; Riahi, H.T. Dynamic response of structures subjected to pounding and structure–soil–structure interaction. *Soil Dyn. Earthq. Eng.* **2015**, *78*, 46–60. [CrossRef]
48. Vicencio, F.; Alexander, N.A. Seismic Structure-Soil-Structure Interaction between a pair of buildings with consideration of rotational ground motions effects. *Soil Dyn. Earthq. Eng.* **2022**, *163*, 107494. [CrossRef]
49. Vicencio, F.; Alexander, N.A. Seismic evaluation of Site-City interaction effects between city blocks. *Front. Built Environ.* **2024**, *10*, 1403642. [CrossRef]
50. Tian, Y.; Lu, X.; Huang, D.; Wang, T. SCI effects under complex terrains: Shaking table tests and numerical simulation. *J. Earthq. Eng.* **2023**, *27*, 1237–1260. [CrossRef]
51. Pirizadeh, M.; Fattahi Kaslani, A.; Keyhani, R. Assessing issues on the seismic response of underground metro station buildings for the vision of seismic-resilient cities: A case study. *Nat. Hazards Rev.* **2026**, *27*, 05026005. [CrossRef]
52. Liu, T.; Liu, K.; Zhang, J. Unstructured grid method for stress wave propagation in elastic media. *Comput. Methods Appl. Mech. Eng.* **2004**, *193*, 2427–2452. [CrossRef]
53. Clough, R.W.; Penzien, J. *Dynamics of Structures*, 3rd ed.; Computers & Structures, Inc.: Berkeley, CA, USA, 1995.
54. *GB 50011-2010*; Code for Seismic Design of Buildings. China Architecture & Building Press: Beijing, China, 2014.
55. Gudainiyan, J. Comparative analysis of response of BI building with varying post yield stiffness ratio under NF and FF ground motion. *Asian J. Civ. Eng.* **2026**, 1–15. [CrossRef]
56. Krawinkler, H.; Seneviratna, G. Pros and cons of a pushover analysis of seismic performance evaluation. *Eng. Struct.* **1998**, *20*, 452–464. [CrossRef]
57. Elnashai, A.S.; Di Sarno, L. *Fundamentals of Earthquake Engineering: From Source to Fragility*; Wiley: New York, NY, USA, 2015.
58. Schwan, L.; Boutin, C.; Padrón, L.A.; Dietz, M.S.; Bard, P.Y.; Taylor, C. Site-city interaction: Theoretical, numerical and experimental crossed-analysis. *Geophys. J. Int.* **2016**, *205*, 1006–1031. [CrossRef]
59. Dominguez, J. *Boundary Elements in Dynamics*; Computational Mechanics Publications: Southampton, UK, 1993.
60. Delépine, N.; Lenti, L.; Bonnet, G.; Semblat, J.F. Nonlinear viscoelastic wave propagation: An extension of Nearly Constant Attenuation models. *J. Eng. Mech.* **2009**, *135*, 1305–1314. [CrossRef]
61. Emmerich, H.; Korn, M. Incorporation of attenuation into time-domain computations of seismic wave fields. *Geophysics* **1987**, *52*, 1252–1264. [CrossRef]
62. Jin, Y.; Jeong, S.; Kim, D. Prediction of dynamic behavior of large-scale ground using 1 g shaking table test and numerical analysis. *Materials* **2023**, *16*, 6093. [CrossRef]
63. Chen, S.; Li, X.; Zhang, H.; Chen, G.; Liu, A.; Du, X. Vision-based displacement test method for high-rise Building Shaking Table Test. *J. Vibroeng.* **2015**, *17*, 4057–4068.
64. Jiang, G.; Xu, X.; Chen, G.; Liu, Y.; Fukahata, Y.; Wang, H.; Yu, G.; Tan, X.; Xu, C. Geodetic imaging of potential seismogenic asperities on the Xianshuihe-Anninghe-Zemuhe fault system, southwest China, with a new 3-D viscoelastic interseismic coupling model. *J. Geophys. Res. Solid Earth* **2015**, *120*, 1855–1873. [CrossRef]
65. Song, J.; Yang, H.; Yao, H. High-resolution seismicity and ground motion variability across the highly locked southern Anninghe fault with dense seismic arrays and machine learning techniques. *J. Geophys. Res. Solid Earth* **2024**, *129*, e2024JB029479.
66. He, H.; Ikeda, Y. Faulting on the Anninghe fault zone, Southwest China in Late Quaternary and its movement model. *Acta Seismol. Sin.* **2007**, *20*, 571–583. [CrossRef]
67. Mu, X.; Song, J.; Yang, H.; Huang, J.; Yao, H.; Tian, B. High-resolution shallow structure along the Anninghe Fault Zone, Sichuan, China, constrained by active source tomography. *Seismol. Res. Lett.* **2024**, *95*, 408–420. [CrossRef]
68. Liu, Y.; Yao, H.; Zhang, H.; Fang, H. The community velocity model v.1.0 of southwest china, constructed from joint body- and surface-wave travel-time tomography. *Seismol. Res. Lett.* **2021**, *92*, 2972–2987. [CrossRef]
69. Zhong, W.; Liu, T. A mesh grading technique for near-fault seismic wave propagation in large velocity-contrast viscoelastic earth media. *J. Earthq. Eng.* **2022**, *26*, 1388–1415. [CrossRef]
70. Wang, G.; Zhou, X. 3D finite-difference simulations of strong ground motions in the Yanhuai area, Beijing, China during the 1720 Shacheng earthquake (M_s 7.0) using a stochastic finite-fault model. *Soil Dyn. Earthq. Eng.* **2006**, *26*, 960–982. [CrossRef]
71. Ye, L.P.; Lu, X.Z.; Ma, Q.L.; Cheng, G.Y.; Song, S.Y.; Miao, Z.W.; Pan, P. Study on the influence of post-yielding stiffness to the seismic response of building structures. In Proceedings of the 14th World Conference on Earthquake Engineering, Beijing, China, 12–17 October 2008.
72. Moczo, P.; Robertsson, J.O.A.; Eisner, L. The finite-difference time-domain method for modeling of seismic wave propagation. *Adv. Geophys.* **2007**, *48*, 421–516.
73. Robertsson, J.O.A.; Blanch, J.O.; Symes, W.W. Viscoelastic finite-difference modeling. *Geophysics* **1994**, *59*, 1444–1456. [CrossRef]
74. Jousset, P.; Neuberg, J.; Jolly, A. Modelling low-frequency volcanic earthquakes in a viscoelastic medium with topography. *Geophys. J. Int.* **2004**, *159*, 776–802. [CrossRef]

75. Christensen, R.M. *Theory of Viscoelasticity: An Introduction*; Academic Press: New York, NY, USA, 1982.
76. Bathe, K.J.; Wilson, E.L. *Numerical Methods in Finite Element Analysis*; Prenttice-Hall, Inc.: Upper Saddle River, NJ, USA, 1976.

Disclaimer/Publisher's Note: The statements, opinions and data contained in all publications are solely those of the individual author(s) and contributor(s) and not of MDPI and/or the editor(s). MDPI and/or the editor(s) disclaim responsibility for any injury to people or property resulting from any ideas, methods, instructions or products referred to in the content.